J. Fluid Mech. (2009), *vol.* 630, *pp.* 225–265. © 2009 Cambridge University Press
doi:10.1017/S0022112009006752 Printed in the United Kingdom

Response of supersonic turbulent boundary layers to local and global mechanical distortions

ISAAC W. EKOTO[1], RODNEY D. W. BOWERSOX[2]†, THOMAS BEUTNER[3] AND LARRY GOSS[4]

[1]Sandia National Laboratories, Livermore, CA 94511-9056, USA
[2]Texas A&M University, College Station, TX 77843-3141, USA
[3]DARPA, Arlington, VA 22203-1714, USA
[4]Innovative Scientific Solutions Inc., Dayton, OH 45440-3638, USA

(Received 30 April 2008 and in revised form 9 February 2009)

The response of the mean and turbulent flow structure of a supersonic high-Reynolds-number turbulent boundary layer flow subjected to local and global mechanical distortions was experimentally examined. Local disturbances were introduced via small-scale wall patterns, and global distortions were induced through streamline curvature-driven pressure gradients. Local surface topologies included *k*-type diamond and *d*-type square elements; a smooth wall was examined for comparison purposes. Three global distortions were studied with each of the three surface topologies. Measurements included planar contours of the mean and fluctuating velocity via particle image velocimetry, Pitot pressure profiles, pressure sensitive paint and Schlieren photography. The velocity data were acquired with sufficient resolution to characterize the mean and turbulent flow structure and to examine interactions between the local surface roughness distortions and the imposed pressure gradients on the turbulence production. A strong response to both the local and global distortions was observed with the diamond elements, where the effect of the elements extended into the outer regions of the boundary layer. It was shown that the primary cause for the observed response was the result of local shock and expansion waves modifying the turbulence structure and production. By contrast, the square elements showed a less pronounced response to local flow distortions as the waves were significantly weaker. However, the frictional losses were higher for the blunter square roughness elements. Detailed quantitative characterizations of the turbulence flow structure and the associated production mechanisms are described herein. These experiments demonstrate fundamental differences between supersonic and subsonic rough-wall flows, and the new understanding of the underlying mechanisms provides a scientific basis to systematically modify the mean and turbulence flow structure all the way across supersonic boundary layers.

1. Introduction

1.1. *Research objective and approach*

Improved understanding of the underlying physical processes associated with mechanically distorted turbulent supersonic boundary layers with surface roughness

---

† Email address for correspondence: bowersox@aeromail.tamu.edu

has many applications including re-entry vehicle thermal protection and internal aeropropulsive flows. Relevant surface topologies range from random pitting, spalting and contamination deposits, to periodic elements associated with tiled thermal protection systems and ablative thermal protection systems with an underlying honeycomb structure. In high-Reynolds-number supersonic turbulent boundary-layer flows, the sonic point, the point above which the flow is supersonic, is close to the surface. Thus, moderate-sized roughness elements may extend into the supersonic portion of the boundary layer, causing corresponding shock and expansion waves that can alter the mean and turbulence flow structure in a manner qualitatively different than in subsonic flows.

The objective of the present study was to achieve improved understanding of the underlying physical processes associated with mechanically distorted turbulent supersonic boundary layers with surface roughness. To meet this objective, a series of experiments were performed in a supersonic ($M = 2.87$) high-momentum-thickness-Reynolds-number boundary layer ($Re_\theta = 40\,000$). To provide a complete and relevant basis for analyses, experiments were performed with the same instrumentation for the following cases: (1) zero pressure gradient boundary layer on a smooth wall, (2) zero pressure gradient boundary layer with square, canonical *d*-type, roughness topology, (3) zero pressure gradient boundary layer with diamond shaped *k*-type roughness topology, which produces a strong secondary flow structure through a pattern of attached oblique shocks and expansion waves, (4) favourable pressure gradient boundary layers on a smooth wall, (5) favourable pressure gradient boundary layers with square roughness, (6) favourable pressure gradient boundary layers with diamond roughness, (7) combined favourable then adverse pressure gradient boundary layer on a smooth wall, (8) combined pressure gradient boundary layer with square roughness, and (9) combined pressure gradient boundary layer with diamond roughness. The first two cases provide a canonical background for comparison purposes, where the *d*-type roughness was expected to follow subsonic trends. Case 3 characterized interactions between the local pressure waves and boundary-layer mean and turbulence flow structure. Cases 4, 5 and 7–9 were examined to characterize global distortion effects for comparison to the local gradients in case 3. The favourable pressure gradients in case 6 were selected to isolate and demonstrate the importance of shock–turbulence interactions near the leading edge of the roughness elements. The experiments provided quantification of the effects of mechanical distortions on the mean flow properties and turbulence statistics, structure and production.

This study builds on three basic bodies of knowledge: (1) supersonic rough-wall boundary layers, (2) distorted supersonic turbulent boundary layers, and (3) shock wave–turbulence interactions. The review presented below summarizes the key building blocks for the present study.

1.2. *Supersonic rough wall boundary layers*

The current understanding of high-speed rough-wall mean and surface flow processes is founded, to a large degree, in applying compressibility scaling to the corresponding low-speed incompressible database (e.g. see Liepmann & Goddard 1957; Goddard 1959; Morkovin 1961; Reda, Ketter & Fan 1975; Berg 1979; Latin & Bowersox 2000, 2002). Incompressible rough-wall boundary layers have been the subject of considerable attention; e.g. see Nikuradse (1933), Perry, Schofield & Joubert (1969), Perry, Lim & Henbest (1987), Schlichting (1955), Ligrani & Moffat (1986), Jimenez (2004), Shockling, Allen & Smits (2006) and Schultz & Flack (2007). These studies have shown that surface roughness has a direct effect on the inner region of the

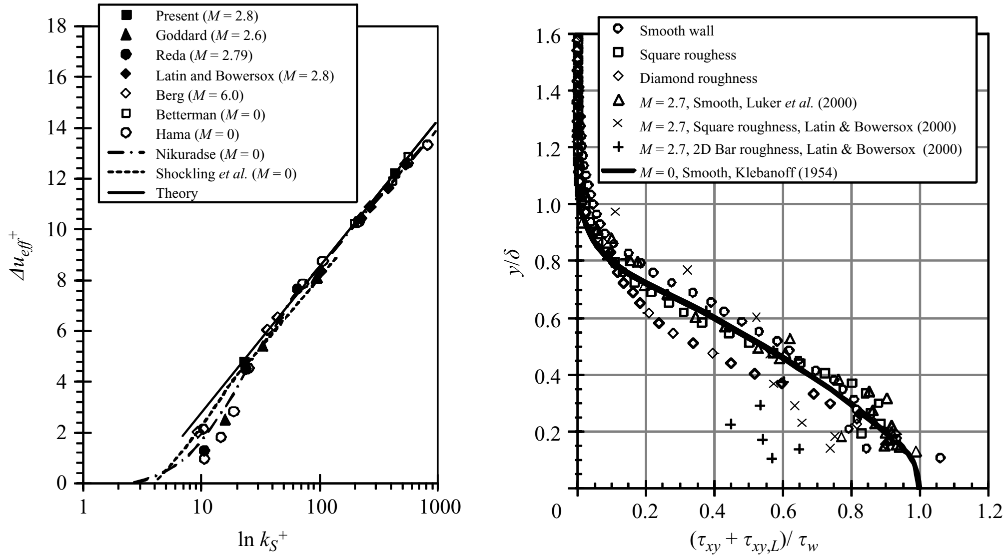

(*a*) Velocity shift.

(*b*) Shear stresses.

FIGURE 1. High-speed mean flow properties (Theory: $B = 5.5$, $C = 8.5$, $\kappa = 0.4$).

law of the wall and is often described by the single roughness Reynolds number parameter. Nikuradse (1933) demonstrated that for low-speed flows, sand-grain generated roughness increased the velocity defect and skin friction, and shifted the velocity law of the wall plot downward. The amount of downward shift was shown to be a function of the roughness height Reynolds number k^+. Nikuradse's data (1933) showed no measurable effect of roughness for k^+ less than about 5–7, a condition commonly referred to as hydraulically smooth. On the other hand, for k^+ greater than about 60–70, the frictional losses and the velocity profile were independent of viscosity, and the flow is called fully rough. In the transition regime where $7 < k^+ < 70$, the flow properties depend on both the viscosity and the roughness. The above descriptions were developed for tightly packed sand grain roughness. Schlichting (1955) developed an equivalent sand grain roughness k_S to relate other roughness topologies to the sand grain roughness. The relation between the actual roughness height and the equivalent sand grain height is $\ln k_S/k = \kappa(8.5 - C)$, where C is the intercept for the actual roughness ($\Delta u^+ = \kappa^{-1} \ln k^+ + B - C$). Generally, the location of the profile origin is selected somewhere between the base and top of the elements to improve the quality of the velocity profile in the logarithmic layer (Perry *et al.* 1969).

Goddard (1959) demonstrated that the sand grain roughness velocity shift for high-speed flow collapsed onto the incompressible correlation when van Driest II (1951) scaling was employed; that is $\Delta u^+_{eff} = \kappa^{-1} \ln k^+_S + B - C$, where u_{eff} is the velocity with van Driest II scaling. Goddard (1959) also found that, for fully rough sand grain flow, C matched the low-speed value of 8.5 with van Driest II scaling. The compilation of the velocity shift data shown in figure 1(*a*) confirms Goddard's conclusion.

The equivalent sand grain description has proven inadequate to characterize roughness topology effects. Hence, investigations of the influence of the roughness geometry have also been performed (Perry *et al.* 1969; Simpson 1973; Antonia & Wood 1975; Bons *et al.* 2001; McClain, Hodge & Bons 2003); Jimenez 2004. Overall, a general description has not been developed. However, two categories of roughness elements have been defined: *k*-type and *d*-type. For *k*-type roughness elements, the equivalent sand grain height is proportional to the roughness height, where for *d*-type, the equivalent sand grain height is proportional to the boundary-layer height (Jimenez 2004). The solidity (Schlichting 1955) is often used as a correlating parameter. However, different definitions have been proposed in the papers listed above.

Raupach, Antonia & Rajagopalan (1991) provide a comprehensive survey (157 papers) of low-speed scaling for laboratory and atmospheric scale flow fields. They extended the Reynolds number similarity concept of Townsend (1976) to include rough walls by defining wall similarity as the boundary-layer turbulent motions outside the roughness or viscous sublayer at high Reynolds numbers that are independent of wall roughness and viscosity. The exceptions were the role of the wall in setting the friction velocity, effective origin and boundary-layer thickness. Raupach *et al.* also pointed out that an important consequence of the wall similarity hypothesis is that the organized structures (double-roller eddy or Λ-vortex) in the outer region of the rough-wall boundary layers should be the same as those for smooth wall boundary layers, even though the near-wall vortex generation for smooth and rough walls is fundamentally different. Smooth walls are characterized by the bursting process and rough surfaces by organized wake vortices. For most roughness types, the near-wall flow is so disturbed that the smooth wall low-speed streaks are eradicated; however, there is evidence of a rough-wall counterpart (Raupach *et al.* 1991). Grass (1971) performed detailed investigations of the influence of surface roughness on the turbulent structure and turbulence production. His data confirmed that the smooth wall inrush and ejection process, typically associated with the bursting process, correlate with a high contribution to the Reynolds stress and hence turbulence production close to the wall. The inrush and ejection process was found to be present irrespective of the surface roughness condition. Grass also noted a strong interaction between the inner and outer flows. In a recent experimental study, George & Simpson (2000) resolved the flow around the roughness elements and obtained data very close to the wall. These data show that the near-wall structure was highly dependent on the roughness topology. However, the outer region, when scaled by the friction velocity, was independent of the roughness, which further confirmed the conclusions of Raupach *et al.* (1991).

High-speed studies that include turbulence data are less common. The high-speed rough-wall Reynolds shear stress measurements of Latin & Bowersox (2000) are compared to representative low-speed data along with additional high-speed smooth wall data in figure 1(*b*). In figure 1(*b*), $\tau_{xy} = -\bar{\rho}\overline{u'v'}$ and $\tau_w = \rho_w U_\tau^2$. The laminar term, $\tau_{xy,L}$, is only significant near the wall and in the logarithmic region of the boundary layer, $\tau_{xy} \approx \tau_w$. The scatter in the data in this plot is representative of the current database (e.g. see the compilations in Dussauge *et al.* 1996). The supersonic smooth wall data of Luker, Bowersox & Buter (2000) and the supersonic sand grain and square roughness topology roughness data of Latin & Bowersox (2000) also followed Townsend's (1976) scaling, with Morkovin's $\bar{\rho}/\rho_w$ scaling (1961). However, the two-dimensional bar roughness element topology studied by Latin & Bowersox (2000) did not follow the pattern. These data indicated a dependence of outer-region turbulent levels on the roughness topology. Latin & Bowersox (2000) also found that the correlation between transverse velocity and density fluctuations ($\overline{\rho' v'}/\overline{\rho u}$), directly measured by combining the response from hot-wire anemometry with laser Doppler velocimetry, demonstrated a systematic dependence on the roughness height. This was the general conclusion for all of the turbulence properties that included a thermodynamic variable. They believed this dependence was the result of the roughness elements generated by shock and expansion waves interacting with the boundary-layer turbulence. The present study showed that secondary distortions associated with such waves significantly affect the transport of turbulence.

1.3. *Distorted supersonic turbulent boundary layers*

Curvature-driven bulk compression and dilatation is important to the present study on both the local and global scales. Considerable theoretical and experimental studies have been performed to characterize the response of supersonic boundary layers to bulk compression/dilatation (e.g. see Bradshaw 1969, 1974; Dussauge & Gaviglio 1987; Smits *et al.* 1989; Smith & Smits 1991; Smits & Dussauge 1996; Spina, Smits & Robinson 1994; Arnette *et al.* 1996 and Luker *et al.* 2000). The data compiled in Spina *et al.* (1994) show that adverse pressure gradients and/or concave wall curvature result in destabilized flow with amplified turbulence levels, where favourable pressure gradients and convex wall curvature have a stabilizing effect. Bradshaw's (1974) distortion (d) parameter, defined as the ratio of the sum of the secondary strain rates to the primary velocity gradient normal to the wall, is often used to characterize the strength of the pressure gradient. A distortion is generally considered mild if $d < 0.01$ and strong if $d > 0.1$. Bradshaw also pointed out that the effect of the extra strain rates on the turbulence properties is an order of magnitude stronger than implied by the extra production alone. Spina *et al.* (1994) utilized two impulse parameters to characterize the imposed distortion strength: the bulk dilatation impulse parameter, defined as $I_p = \gamma^{-1} \ln p_2/p_1$, where subscripts '1' and '2' correspond to the pressure before and after the imposed pressure gradient, and the streamline curvature parameter given by $I_\phi = \Delta\phi$, where ϕ is the change in the wall angle in radians. Imposed impulses of $I_p = 0.5$ and 0.8 produced 200 % and 600 % increases in the axial turbulent shear stress intensities, respectively. Wall curvature was found to further enhance the amplifications. The studies of Arnette *et al.* (2000) and Luker *et al.* (2000) demonstrated that axial turbulence intensity reductions of up to 90 % were possible for imposed wall-induced favourable pressure gradients. Near the wall, turbulent shear stress reductions of up to 75 % were observed, and in the outer half of the boundary layer, the turbulent shear stresses were negative, while the principal strain rate remained positive. Luker *et al.* (2000) experimentally demonstrated that the associated extra production terms because of the induced strain rates resulted in overall negative turbulence production in the same region of the boundary layer. Luker *et al.* (2000) also inferred from their data that the favourable pressure gradient flow led to large-scale eddy disintegration, resulting in increased turbulent energy available for flow dissipation and the observed stabilizing effect on the boundary layer. The present study demonstrated that the trends cited for the global distortions also hold for small-scale local distortions in supersonic flows.

1.4. *Shock–turbulence interaction*

Shock–turbulence interaction is important to the present study on a local scale as the present surface topology produced local shock waves. As described by Mahesh, Lele & Moin (1995), shock–turbulence interaction has numerous practical applications. Hence, considerable theoretical, experimental and numerical research has been performed to characterize the response of turbulence as it passes through a shock wave (Keller & Merzkirch 1990; Dolling 1990; Jacquin, Cambon & Blin 1993; Mahesh, Lele & Moin 1993, 1997; Mahesh *et al.* 1995; Thivet *et al.* 2001; Sinha,

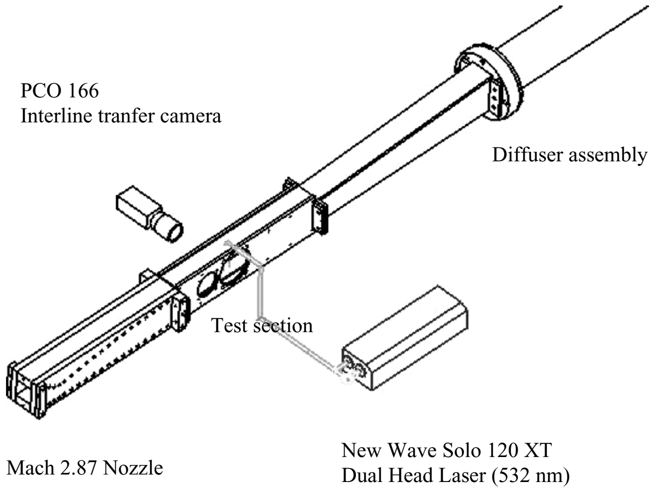

FIGURE 2. Schematic of supersonic wind tunnel (flow is up and to the right).

Mahesh & Candler 2003, 2005). One of the major interests for the present study is the shear stress; i.e. the anisotropic portion of the stress tensor. Recent computational models (Wallin & Johansson 2000) relate the standard anisotropic portion of the Reynolds stress tensor to the mean strain-rate tensor relation augmented by higher-order strain and rotation-rate tensors. Additionally, Mahesh *et al.* (1993) demonstrated that the evolution of the Reynolds shear stress in an anisotropic shear layer was strongly dependent on the angle between the compression and shear layer. Since the stress tensor can be diagonalized through the choice of an appropriate coordinate system, i.e. the principal axes, there is no inherent distinction between the normal and shear stresses, only between the isotropic and anisotropic portions of the stress tensor (Miles 2007, personal communication), and the principal axes should be heavily biased towards the orientation of a shock wave. The important parameters needed to describe the turbulence stress evolution are the angle (α) necessary to rotate the normal stresses to their principal axes and the turbulent kinetic energy (k^T), which remains constant regardless of orientation. Mahesh *et al.* (1997) demonstrated that the sign of the correlation between the axial velocity fluctuation and the temperature fluctuations, that is $\overline{u'T'}$, had an important impact on the role of the shock–turbulence interaction. If $\overline{u'T'} < 0$, then the amplification of the turbulence levels (kinematic and thermodynamic) across the shock is enhanced. This is the case for adiabatic supersonic turbulent boundary layers. However, if $\overline{u'T'} > 0$ upstream of the shock, which would be the case for a highly cooled wall, then the amplification of the kinetic energy is strongly suppressed. Mahesh *et al.* (1997) also demonstrated that the phase difference between the upstream vorticity and entropy waves determines whether amplification occurs. It was demonstrated in the present study that roughness element shock waves enhanced the turbulence levels through this interaction mechanism.

2. Facilities and diagnostic test equipment

2.1. *Wind tunnel*

The experiments were performed in a supersonic wind tunnel located at Texas A&M University. A schematic of the wind tunnel is given in figure 2. The facility was operated in a blow-down mode, with a maximum nominal run time of 20 min. The free-stream Mach number (M) at the nozzle exit was 2.87 with a ±1.0 % variation across nozzle exit core flow. The nozzle exit dimensions were 7.62×7.62 cm. The stagnation pressure and temperature were set to 690 kPa (±5.0 %) and 315 K (±3.5 %), respectively. At the operating stagnation temperature, the adiabatic wall temperature was approximately equal to the ambient temperature in the laboratory, which, when coupled with the relatively low thermal conductivity of the Plexiglas floors in the tunnel, resulted in minimal wall heat transfer.

A Pitot probe with an Omega brand PX303 pressure transducer (0–690 kPa and ±0.25 % full-scale accuracy) was used to monitor the stagnation pressure within the settling chamber. The total temperature was measured using an Omega brand JQSS thermocouple amplified by an OMNI AMP-IV thermocouple amplifier. Tunnel static pressure was measured with five Omega brand PX303 pressure transducers (0–103 kPa and ±0.25 % full-scale accuracy). Data from the pressure transducers and thermocouples were collected with a Keithley brand KPCI-3110 data acquisition board with a sampling rate of 1.25 MS s^{-1}. The board had 12 bit resolution.

Measurements took place in the floor boundary layer of the wind tunnel. The test section was located just downstream of the nozzle exit (see figure 2). Owing to the half block design, the floor boundary layer experienced 20.5 cm of constant pressure flow in the axial direction at the free-stream conditions before reaching the test section entrance. The boundary-layer thickness δ_{ref} at the nozzle exit was 1.0 cm.

2.2. *Roughness topologies*

Two roughness topologies were designed to produce fundamentally different near-wall distortions. Smooth wall models were also tested for comparison purposes. The models were manufactured from Plexiglas and polished using Mothers 05100 Mag and Aluminum Polish. The estimated roughness height, k^+, for the smooth models was 0.14.

A square roughness topology was designed to produce the canonical 'sand-grain' behaviour observed in low-speed flow. More specifically, Latin & Bowersox (2000) demonstrated that the three-dimensional machined square topologies followed the accepted correlations (see figure 1*b*). To further foster the accepted scaling, the roughness elements spacing was selected to produce the *d*-type roughness characteristic. Perry *et al.* (1969) remarked that for *d*-type periodic roughness elements, recirculation is set up in the grooves and eddy shedding from the elements into the flow is negligible. For the zero-pressure-gradient smooth wall model, the law-of-the-wall with van Driest II (1951) scaling indicated that the sonic line was nominally 0.12 mm above the wall. For the rough wall, it was desired to have a fully rough topology, while maintaining the roughness height below the sonic line to minimize roughness element-induced shock-wave generation. With the correlation in figure 1(*a*), the roughness height was selected at 0.8 mm. At this *y*-location, the local Mach number was estimated at 0.9. Thus, strong localized shock waves were not expected for this roughness topology. Instead, the roughness was expected to produce enhanced momentum loss similar to that for low-speed flows. The model was machined from Plexiglas. The channels were created using a 1.6 mm diameter ball end mill bit. These were 0.8 mm deep, creating roughness elements with a length and width of 1.6 mm, and separated from adjacent elements by a 1.6 mm wide channel. A schematic of the element shape is given in figure 3(*a*), while the expected flow structure is illustrated in figure 4(*a*). The flow for this roughness topology was expected to follow the canonical

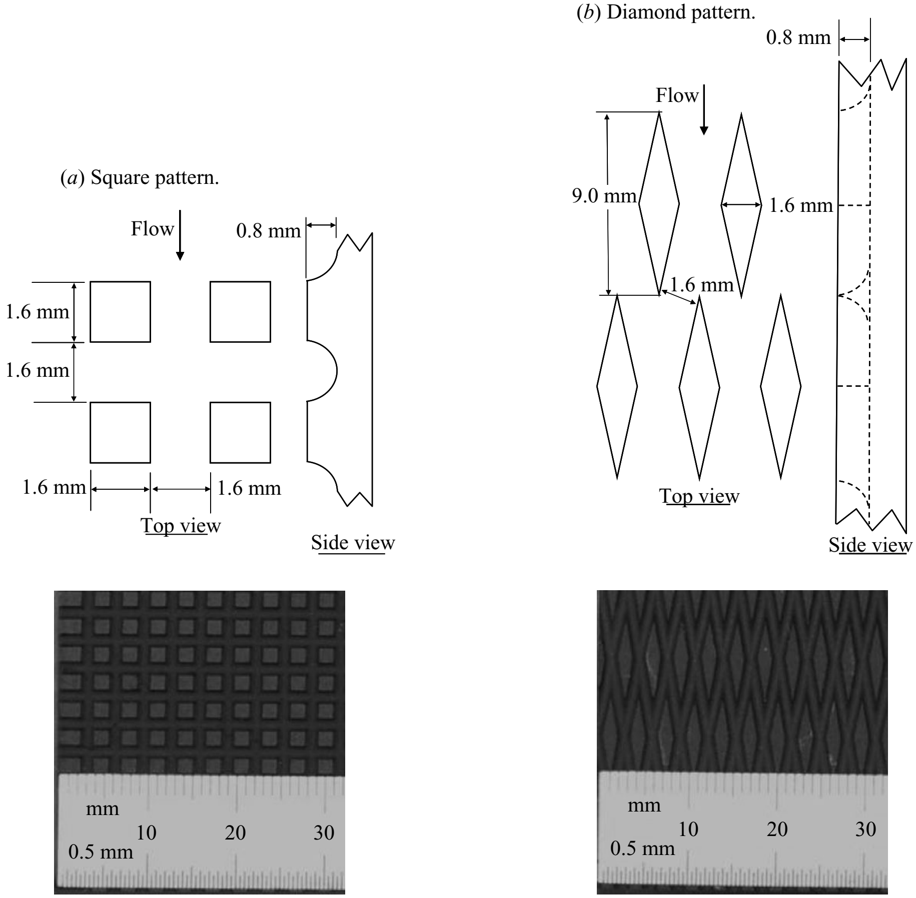

FIGURE 3. Roughness topology.

mean and turbulent patterns observed by Goddard (1959) and Latin & Bowersox (2000), respectively.

The diamond roughness topology was selected so that the height and frontal blockage closely matched the square roughness elements. The diamond roughness, however, induced significant localized shock and expansion flow distortions by way of attached leading edge oblique shock waves, followed by Prandtl–Meyer expansions. The diamond elements were 9.0 mm long, 1.6 mm wide and 0.8 mm tall. The major axis of the roughness element was aligned with the flow direction, and the leading edge had a 10° half-angle. A schematic of the element shape is given in figure 3(*b*), while the expected flow structure is illustrated in figure 4(*b*). As indicated in figure 4(*b*), the flow was expected to wrap around the elements, thus exposing more of the topology to the supersonic crossflow. If the entire element was exposed to the flow, then the average local Mach number at the element height would have been 1.3. Since the boundary layer was adiabatic, the shock–turbulence interaction was expected to be similar to case 1B in Mahesh *et al.* (1997).

2.3. *Pressure gradients*

Two pressure gradient models were designed to provide significant pressure gradient/streamline curvature effects. Expansion and compression wave theories

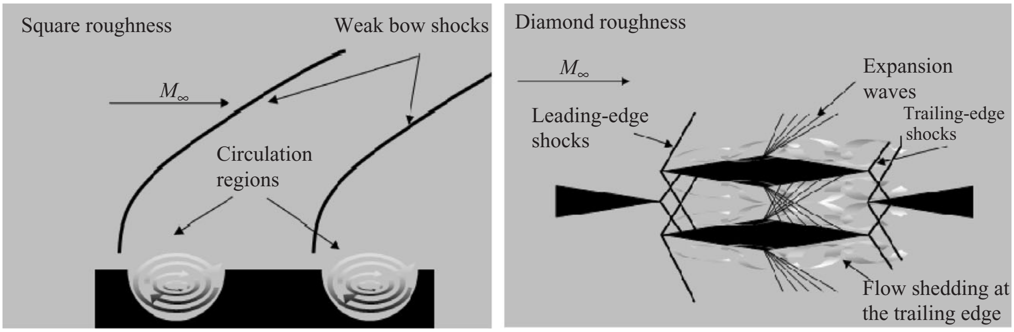
(*a*) Square pattern.

(*b*) Diamond pattern.

FIGURE 4. Sketch of the square (side view) and diamond (the top view) roughness element flow patterns.

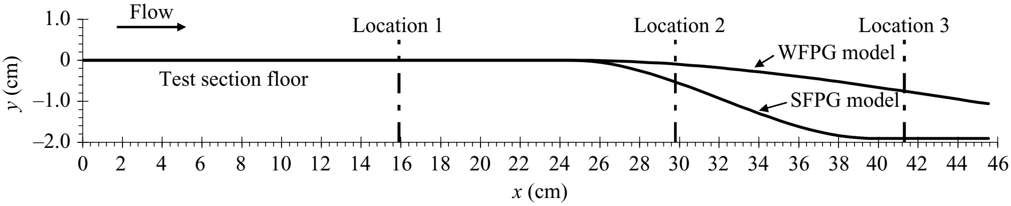

FIGURE 5. Sketch of streamline curvature wall geometry.

	x_1 (cm)	x_2 (cm)	A	B
WFPG	24.54	63.54	6.423×10^{-5}	-8.757×10^{-3}
SFPG	24.54	39.64	1.107×10^{-3}	-2.507×10^{-2}

TABLE 1. Model geometry and pressure gradient parameters.

were used to estimate the values of the distortions and impulse parameters for the global pressure gradients. The weak favourable pressure gradient (WFPG) model was designed to provide a small perturbation, and the strong favourable pressure gradient (SFPG) model produced a more pronounced effect, where the imposed global gradient was of similar magnitude but opposite sign to the adverse gradient on the front half of the diamond surface element. The combined local and global gradients were chosen to help isolate the shock–turbulence interaction effects. The pressure gradient models were similar to those used by Luker *et al.* (2000). The curved walls were machined to match the following polynomial: $y = A(x - x_1)^3 + B(x - x_1)^2$, where x_1 is the axial location where the curvature begins. The beginning and end locations for the wall curvature, along with the polynomial coefficients, are listed in table 1. A schematic, with the coordinate system, is given in figure 5. A flat wall was used to approximate a zero pressure gradient (ZPG) flow. In addition to the favourable pressure gradient region, measurements were also acquired just downstream of the compression region for the strong favourable pressure gradient model, which will be referred to as the combined pressure gradient (CPG) region.

2.4. *Coordinate system and measurement locations*

A wind axes Cartesian coordinate system was adopted, where the origin was located on the floor at the centre of the test section entrance. The coordinates in figure 5 correspond to the adopted system. The roughness element plates started at $x = 0$. Measurements were centred on three locations: $x = 15.9$ cm, 29.8 cm and 41.3 cm (as shown in figure 5). For orientation purposes, the leading edge of the 18th row of diamond elements for all of the models was located at $x = 15.5$ cm. This location corresponded to the 49th row of square roughness elements.

2.5. *Schlieren photography*

A Z-type 2-mirror Schlieren system was used. The knife-edge was aligned for density gradients normal to the wall. The Schlieren image was recorded by a Nikon D50 SLR digital camera.

2.6. *Pressure-sensitive paint*

Surface pressure distributions were documented using pressure sensitive paint (PSP) (Liu & Sullivan 2005). The paint used in the present tests was a UNC405 produced by Innovative Scientific Solutions Inc. (ISSI). The binary paint was designed for a pressure range of 10 and 150 kPa, which covered the surface pressures in this study. Six coats, each approximately 10 μm thick, were sprayed onto each test section model. The models were cured with a heat gun for approximately 15 min after the final coat was applied. An ISSI Inc. lm series LED array light source was used to excite the PSP, and a PCO 1600 camera was used to image the luminescence over 5.08 cm × 3.81 cm area. The 1600 × 1200 camera resolution was reduced to 800 × 600 via pixel binning for enhanced signal-to-noise ratio.

OMS Lite version 1.1 by ISSI was the software package used to process the PSP images. The software was capable of resolving errors due to photo-detector noise, non-uniform image illumination and model deformation by using a two-dimensional displacement evaluation which included image registering. For each run, four images were acquired: a background image without ambient illumination, an initial wind-off image taken just before the tunnel was started and with the LED array on, a wind-on image with the tunnel running long enough to reach thermal equilibrium, and a final wind-off image taken immediately after the tunnel was stopped. To account for model distortions, eight marker dots were applied to the surface with a felt tip pen at known locations. The location of each marker dot was entered into the OMS software and image registration was accounted for using an eight-step quantum pixel energy distribution (QPED) algorithm as described by Navarra *et al.* (2001) with three iterations and an initial box size of 16 × 16 pixels. Due to the paint's thermal and pressure dependence, the PSP was calibrated by a second-order least-squares approximation with known temperatures and pressures. Finally a 4-pixel box smoothing filter was applied to sharpen the linear interpolation of PSP values. Comparisons were made on the smooth model, and the PSP values were within 1.0 % of the pressure tap data. However, because of the small size of the roughness elements, it was not possible to resolve the pressure on the surface of the elements or within the channels using static pressure ports. The measurement uncertainty analyses for the PSP, as well as the remaining diagnostic methods, are summarized in § 2.9.

2.7. *Pitot pressure*

The Pitot pressure was measured with an Omega brand PX303 pressure transducer (0–690 kPa, and ±0.25 % full-scale accuracy). The pressure probe had a 1.6 mm diameter tube with an inner diameter of 0.8 mm. The end of the tube was crimped so that the entrance height was 0.2 mm. The probe was traversed in the floor-normal direction by a Velmex model MA2508P40 linear translation stage that contained a turn screw that had 15.75 turns per centimetre. The translation stage was moved by a Vexta PK2608-02A 400-step stepper motor. The stepper motor was operated by an S100 3-channel stepper motor controller which was controlled by a PC running the S100 SMC software. The probe was translated at 1.9 cm per minute. The position of the probe was monitored with a P3 America Inc. ISDG linear variable displacement transducer (0–20 mm and ±0.5 % full-scale accuracy). Probe pressures were sampled at a rate of 1.0 kHz, and each data point was the result of a 100-point average.

2.8. *Particle image velocimetry*

Particle image velocimetry was used to measure velocity fields across the boundary layer with sufficient spatial resolution to resolve the flow over the roughness elements. For the present tests, the tunnel was seeded by a TSI Six-Jet Atomizer Model 9306 with Bertolli extra light olive oil. The documented mean particle diameter was 0.6 μm, and the 3 dB frequency response of the particles was documented at 60–200 kHz (Bowersox 1996). Tracer particles were illuminated via Mie scattering from laser radiation supplied by a dual port/dual head New-Wave Solo 120XT PIV laser. Each laser head had a maximum energy output of 120 mJ at 532 nm, 4 ns pulse width and a maximum rep rate of 15 Hz. To minimize laser energy losses during beam collimation, the beam out of the second port was cross-polarized using a crystal quartz half-wave plate, and collimated using a high-energy polarizing cube beam splitter that provided efficient narrowband polarization. A BK7 spherical lens ($f = 500$ mm) was used to create a nominally 500 μm thick laser sheet, above the test section floor. The sheet width was around 3.0 cm, and was formed using a BK7 Plano-concave cylindrical lens ($f = -75$ mm). The laser sheet was located along the lateral centreline of the wind tunnel. The camera used was a Cooke Corp. PCO 1600 interline-transfer CCD camera equipped with a Nikon 60 mm lens. The camera trigger, laser Q-switch and laser flashlamp were all controlled by a Quantum Composers Model 9618 pulse generator. The camera frame grabbing software was Camware version 2.13.

Velocity fields were created using the ISSI brand dPIV 32-bit analysis code. For the present measurements, a three-step adaptive cross-correlation was used, with successive rectangular interrogation sizes of 128×64, 64×32 and 32×16 pixels and a 50 % overlap. In order to enhance the intensity of correlation peaks relative to random noise, a four-map correlation multiplication process filter was used. A consistency post-processing filter was used to improve the adaptive correlation calculation. First- and second-order turbulent statistics were created using an in-house code that ensemble averaged the velocity vector fields. For the present study, 5000 image pairs were acquired at each measurement location. The measurement grid consisted of 71×34 data points, where the axial and transverse separations were 0.71 mm and 0.35 mm, respectively. This resolution was sufficient to compute gradients of the mean and turbulent flow properties across the roughness elements.

2.9. *Measurement uncertainties*

Measurement uncertainties for the present study are summarized in table 2, and were accumulated with a Euclidean (L_2) norm. Uncertainties in stagnation conditions included probe location uncertainty and run-to-run repeatability. The run-to-run repeatability of the PSP was 3.3 kPa. However, the uncertainty between different measurement points for the same run was considerably smaller (∼ 200 Pa). The axial position uncertainty was taken as half the smallest division on the calibration scale, and the Pitot probe transverse probe position uncertainty was taken as approximately

Variable	Error
p_{01},T_{01}	3.0 (kPa), 16 (K)
PSP	3.3 (kPa)[a]
x, y	0.4, 0.1 (mm)[b]
δ	0.7 (mm)[b]
$\bar{u}$	3.8 (m s^{-1})[b]
$U_{eff}{}^{+}$	6.0 %[b]
$\overline{u'u'}$, $\overline{v'v'}$	4.0 %
$\overline{u'v'}$	8.0 %
$\mathrm{d}\bar{u}/\mathrm{d}x$, $\mathrm{d}\bar{u}/\mathrm{d}y$	3.0 %, 8.0 %
$P_{xx}/\bar{\rho}$, $P_{yy}/\bar{\rho}$,$P_{xy}/\bar{\rho}$	20.0 %

[a] Refers to run-to-run repeatability. Spatial uncertainty from the same run was much smaller (200 Pa)

[b] Applies to both Pitot probe and PIV.

Table 2. Uncertainty estimates.

half the probe tip height. Boundary-layer thickness uncertainty accounted for the uncertainties in position and velocity, where the sensitivity to the velocity uncertainty was estimated with a 1/7th power law. The uncertainty analysis of the PIV data accounted for correlation mapping error and the conversion error from the physical length scale to the appropriate number of camera pixels. The axial position uncertainty was the same as that of the Pitot probe. The transverse position uncertainty was taken as that of the wall position, which was known to within 2 pixels (∼0.1 mm) on the camera array. To estimate the uncertainty in the statistical quantities, a 95 % confidence interval was used (Benedict & Gould 1996), with the variance determined assuming a normal distribution of 5000 instantaneous velocity vector fields. The normalized uncertainty analysis was only applicable to the axial velocity because magnitude of the transverse velocity was comparatively very small. Hence, the magnitude of the transverse velocity uncertainty was taken to be the same as that of the axial velocity. The length scale and axial velocity uncertainties for the PIV and Pitot pressure probe were similar. The tabulated fluctuating velocity correlation uncertainty is for the boundary-layer outer region only; near the wall the uncertainties were considerably higher, e.g. $\sim 35\,\%$ at $y/\delta \sim 0.1$. The magnitude of the velocity gradient uncertainty was a combination of the uncertainties in spatial position and mean velocity measurements. The spatial difference uncertainty only accounted for the conversion error from the physical length scale to the PIV image pixels as the offset uncertainties applied to the entire image. The mean velocity uncertainty included the value listed in table 2. Added to the spatial difference uncertainty for y-component derivative was an estimate of the error due to the curvature of the velocity profile within PIV interrogation window. The resulting uncertainty estimates are listed in table 2. The resulting uncertainty for the production was estimated at approximately 20 %.

2.10. *Flow field three-dimensionality*

Elimination of laser reflections off of the roughness elements was a key challenge associated with the present study, where data were acquired along the centreline of the tunnel. For the smooth and square roughness pattern, it was reasonable to assume that the flow statistics were nominally two-dimensional, and thus the laser sheet was

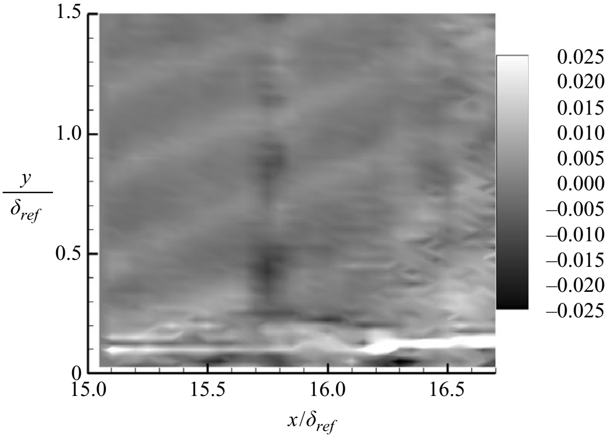

FIGURE 6. Diamond roughness element velocity difference: $(\bar{v}_{mid} - \bar{v}_{side})/U_{ref}$.

located such that wall reflections were minimized. This assumption was questionable for the diamond roughness elements, as localized secondary flows were expected. To estimate the effects of three-dimensionality on the diamond element flow, additional PIV measurements were taken across the span. The first measurements were taken along the centre of the lateral span of a roughness element, while a second data set was acquired at a position shifted 0.4 mm in the z-direction, which was near the midpoint between the element centre and element edge. The shifted data were subtracted from the centreline contours. The transverse velocity difference contour is displayed in figure 6. The dark vertical structure located near $x/\delta_{ref} = 15.75$ and the bright axial structure near $y/\delta_{ref} = 0.15$ were the results of laser reflections. Away from these reflections, the maximum difference was nominally 3.0 m s^{-1}, which was less than the 3.8 m s^{-1} measurement uncertainty listed in table 2. The axial velocity had a similar difference. Therefore, for the present work, the relatively small three-dimensional effects were neglected and the laser sheets were positioned to minimize laser reflections.

3. Overall flow structure

3.1. *Free-stream and surface properties*

The measured flow and surface properties for the present study are summarized in table 3. The free-stream Mach numbers and boundary-layer thicknesses were based on Pitot probe surveys. The wall density and temperature were computed assuming an adiabatic wall. The friction velocity was estimated by assuming that the Townsend (1976) trend, with Morkovin (1961) scaling, shown in figure 1(*b*), held for the zero pressure gradient smooth and *d*-type roughness flows. The present Reynolds shear stress data results for the smooth, square and diamond model cases are included in figure 1(*b*). In this plot, the wall shear was selected to best fit the trend near the wall. It was assumed that the near-wall behaviour, where $\tau_{xy} + \tau_{xy,L} = \tau_w$, was most relevant. The Reynolds shear stress data were averaged axially for a distance of $1.6\delta_{ref}$ to minimize the effects of the local roughness generated by pressure gradients on the wall shear stress estimates. As indicated in figure 1(*b*), the overall shapes of the present smooth and square roughness profiles followed the Klebanoff (1955) trend, as did the smooth wall supersonic data of Luker *et al* (2000). However, the

Model	M_∞	δ mm	U_τ m s^{-1}	ρ_w kg m^{-3}	T_w K	k_s/k	k_s^+
		$x = 15.9$ cm					
ZPG smooth plate	2.85	11	23	0.28	294	0	0
ZPG square roughness	2.82	12	35	0.29	294	0.73	440
ZPG diamond roughness	2.84	11	26	0.28	294	0.07	23

TABLE 3*a*. Flow conditions for zero pressure gradient models.

Model	M_∞	δ mm	ρ_w kg m^{-3}	T_w K
	$x =$ 29.8 cm			
WFPG smooth plate	2.87	13	0.27	294
WFPG square roughness	2.84	14	0.28	294
WFPG diamond roughness	2.87	14	0.27	294
SFPG smooth plate	3.16	16	0.18	292
SFPG square roughness	3.12	17	0.19	293
SFPG diamond roughness	3.14	16	0.18	292
	$x =$ 41.3 cm			
WFPG smooth plate	2.97	16	0.23	293
WFPG square roughness	2.90	17	0.26	294
WFPG diamond roughness	2.94	17	0.24	293
CPG smooth plate	2.77	19	0.31	294
CPG square roughness	2.81	23	0.30	294
CPG diamond roughness	2.81	20	0.30	294

TABLE 3*b*. Flow conditions for non-zero pressure gradient models.

diamond stresses were 30 % below the trend in the outer region of the boundary layer. This difference, like those described by Latin & Bowersox (2000), was due to the influence of the local shocks and expansions on the turbulent shear stresses; these phenomena are described in more detail below. The resulting friction velocities are listed in table 3(*a*).

3.2. *Schlieren photography*

The estimated wall shear stress for the square roughness elements was nearly twice that for the diamond elements. Following Goddard's (1959) arguments, a lower wall shear stress was expected for the more streamlined diamond elements. The corresponding equivalent sand grain heights were computed, as described in § 1.1, and included in table 3(*a*). Wall shear stresses were not estimated for the cases with imposed global distortions (table 3*b*), as the presence of the pressure gradient would have introduced significant uncertainty.

Schlieren photographs were acquired to provide an overall view of the flow structure. Because of optical access limitations, images were restricted to the second station ($x = 29.8$ cm). Examples for the strong favourable pressure gradient model are given in figures 7(*a*) and 7(*b*). The local roughness-induced flow structure for the weak and zero pressure gradient models followed the patterns described below. The flow direction was from left to right and the surface roughness was located along the lower surface. Surface boundary layers in figure 7(*a*) are visible as the dark and light bands along the floor and ceiling, respectively. The dark line angled down to the right emanating from about two-thirds the way up from the bottom left corner was a weak

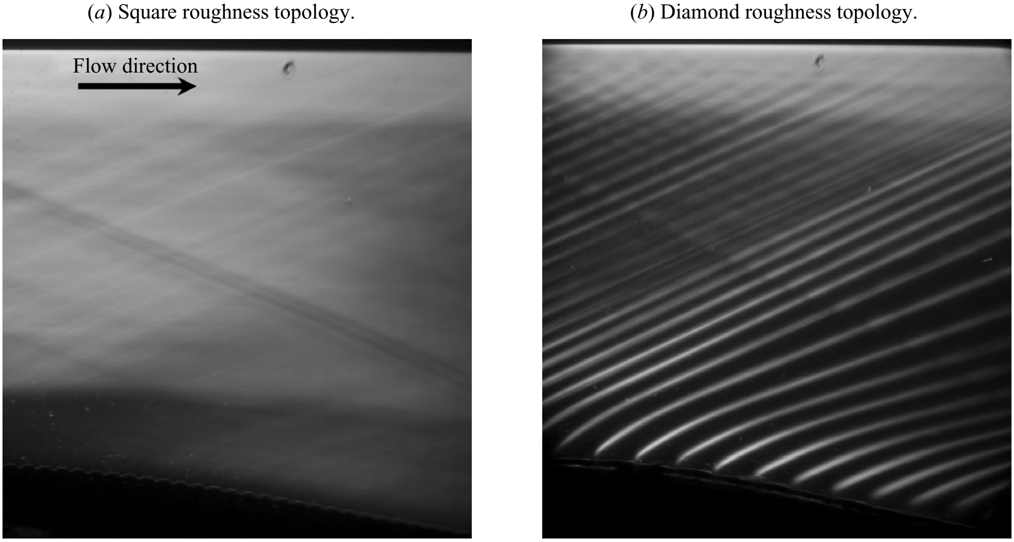

(*a*) Square roughness topology.

(*b*) Diamond roughness topology.

FIGURE 7. Schlieren photograph at second station for strong favourable pressure gradient roughness models.

wave which formed at the intersection of nozzle exit and test section floor, and was too weak to be detected by the quantitative measurements. In addition, faint waves were observed originating from the square roughness elements. The diamond element roughness model (figure 7*b*) produced a significantly different wave structure than was seen for the square roughness model. The shock waves originating from the roughness elements are clearly discernible as the bright curved lines that moved up and to the right. These waves were significantly stronger than those for the square roughness model. The flow expansion for this model was also visible as shock waves spread apart as the flow moved around the wall curvature. The PIV contours (figure 10*b* and *d*) for the diamond element models displayed a wave pattern which corresponded to the wave structure shown in figure 7(*b*); these waves were also present in the Pitot surveys (not shown). These wave patterns were not present in the corresponding square roughness data. These images confirm the presence of roughness element generated by gas dynamic waves.

3.3. *Pressure-sensitive paint*

The PSP data were used primarily to examine the local pressure fields generated by the roughness elements. Examples of surface pressure distributions for the square and diamond roughness patterns are presented in figure 8(*a*) for the zero and strong favourable pressure gradient models, with corresponding line traces of $(P_w - \bar{P}_w)/\bar{P}_w$ for the zero pressure gradient models plotted in figure 8(*b*). For the square roughness topology, a modest 5 % increase in surface pressure was observed within the channels between the roughness element surfaces, while the diamond roughness model PSP image revealed strong alternating adverse and favourable pressure gradients which were not restricted to the interface between the roughness edge and the channels. These data confirmed the expected flow topology shown in figure 4(*b*), where a sketch is overlaid on the PSP image. On the front half of the roughness element, there was an increase in the pressure due to the oblique shock waves. The pressure then decreased on the back half as a result of the expansions. The high- and low-pressure regions from the individual elements overlapped adjacent elements producing pressure

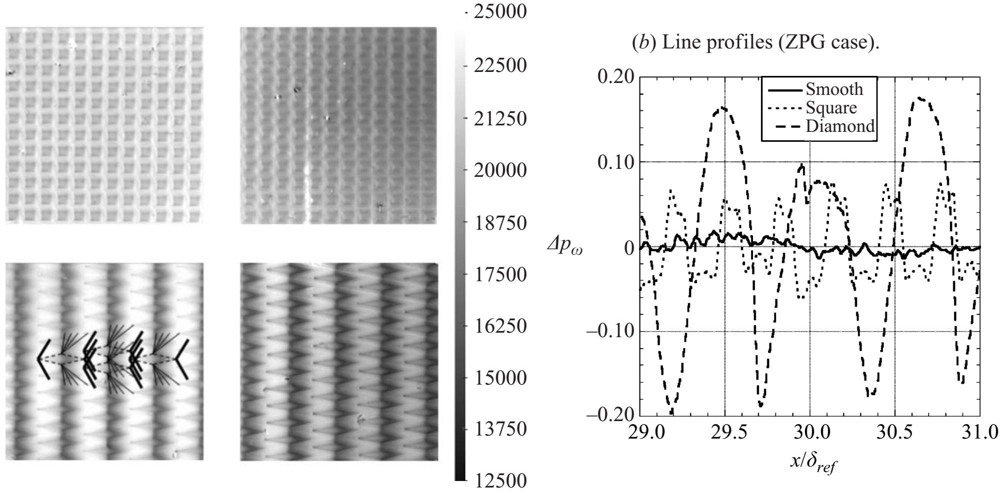

(*a*) ZPG (left) and SFPG (right) roughness pressure contours.

(*b*) Line profiles (ZPG case).

FIGURE 8. Pressure-sensitive paint results.

gradients that exhibited a strong periodic axial variation ($\pm$10 % to 18 % of the mean wall pressure). The amplitude of the pressure rise was found to depend on the position relative to the roughness elements. The two larger peaks at $x/\delta_{ref} = 29.5$ and 30.7 in figure 8(*b*) corresponded to the regions between the leading edges of two adjacent elements, while the smaller one, located at $x/\delta_{ref} = 30.0$, corresponded to the pressure directly on a roughness element. The strong favourable pressure gradient models had similar localized flow structure around the roughness elements, and also exhibited the expected steep decrease in surface pressure in the axial direction. Comparing the left and right images in figure 8(*a*), the noticeable change in greyscale indicates that the global pressure reduction was substantial.

3.4. *Zero pressure gradient inner and outer law-scaled velocity plots*

Law-of-the-wall and defect law plots were constructed for the zero pressure gradient models. The velocity profiles were extracted from the PIV data, and computed from the Pitot data. The Mach number was estimated from the Pitot data using the Rayleigh–Pitot formula, where the static pressure, which was assumed constant, was computed based on the measured free-stream total pressure ratio. Below the sonic point, the Mach number was computed from the ratio of the local total and static pressure using the isentropic relations. The velocity was then estimated assuming a constant total temperature across the boundary layer. Latin & Bowersox (2000) demonstrated the feasibility of this approach for smooth and rough supersonic boundary layers under similar flow conditions. For the present measurements, the planar PIV data were averaged in the axial direction over a range of $\sim 1.6 \cdot \delta_{ref}$, corresponding to 10 square roughness elements, to minimize the effects of the local roughness topology. Smooth and square roughness data were minimally affected by the averaging process, where the scatter was within the measurement uncertainty. However, for the diamond case, the velocity and near-wall Reynolds shear stress varied significantly across the roughness element. Thus, the diamond model velocity data are included in this section for qualitative comparisons only. In addition, the data were not spanwise averaged, further lowering the validity of the diamond model averages.

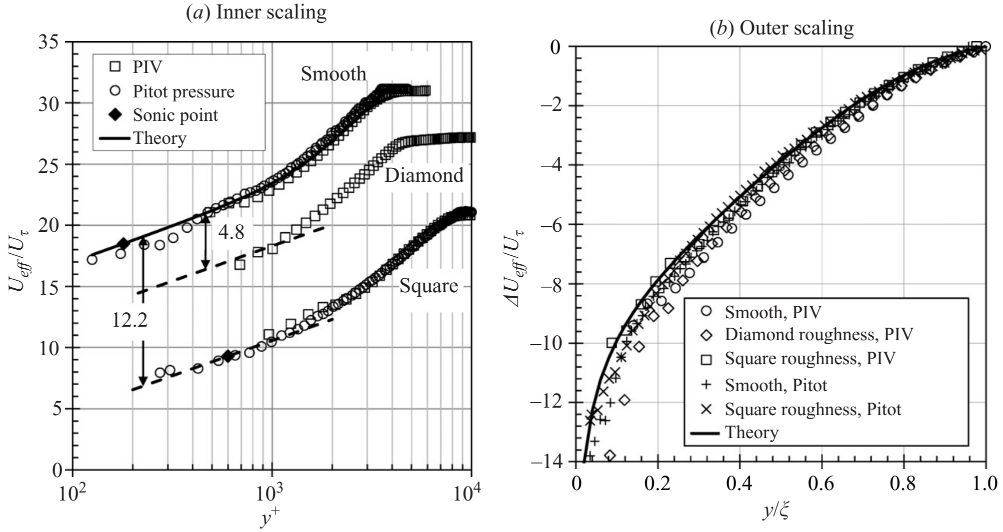

FIGURE 9. Velocity profiles for the zero pressure gradient smooth, square and diamond roughness models.

Plots with inner and outer scaling are displayed in figures 9(*a*) and 9(*b*), respectively. The van Driest II compressibility scaling was also employed, where $B_1 u_{eff}/u_\infty = \sin^{-1}\{[2B_1^2(u/u_\infty) - B_2]/B_3\}_1 + \sin^{-1}(B_2/B_3)$ (where $B_1 = \{(T_{aw} - T_\infty)/T_w\}$, $B_2 = T_{aw}/T_w - 1$ and $B_3 = (4B_1^2 + B_2^2)^{1/2}$). Skin friction was estimated from the PIV turbulence shear stress data as described in §3.1. Smooth model PIV and Pitot data exhibited a good agreement with each other and the law-of-the-wall correlation (figure 9*a*) was given by $\bar{u}_{eff}^+ = \kappa^{-1}\ln y^+ + B + 2\Pi\kappa^{-1}\sin^2(\pi/2 \cdot y/\delta)$, where the constants κ, B and Π were set to 0.4, 5.5 and 1.0, respectively. The square roughness model produced the expected downward shift of the law-of-the-wall for both the PIV and Pitot data, again showing very good agreement with each other. The downward shift was $\Delta\bar{u}_{eff}^+ \approx 12.2$. The diamond model PIV data are also plotted in figure 9(*a*), and the downward shift was estimated at 4.8. This estimate was considered qualitative for the reasons listed in the previous paragraph and because only three data points were present in the logarithmic layer. The intercepts C of $\bar{u}_{eff}^+ = \kappa^{-1}\ln y/k + C$ were 9.3 and 15.0 for the square and diamond roughness models, respectively. The equivalent sand grain heights were then computed following Schlichting (1955), and the results are summarized in table 3(*a*). These data are also plotted in figure 1(*a*); labelled Present ($M = 2.8$). The smooth, axially averaged diamond and square roughness velocity data all collapsed onto the defect-law plot $(\bar{u}_{eff} - \bar{u}_{eff,e})/u^* = \kappa^{-1}\ln(y/\delta) - 2\Pi\kappa^{-1}[1 - \sin^2(\pi/2 \cdot y/\delta)]$, when van Driest II scaling was used (figure 9*b*).

3.5. *Rough wall velocity contours*

Mean velocity contours for the zero pressure gradient square and diamond roughness model are shown in figure 10. The data in figure 10 were representative of all of the zero pressure gradient locations. The velocity components and length scales were normalized by the reference velocity (625 m s^{-1}) and reference boundary-layer thickness (1.0 cm), respectively.

The zero pressure gradient square roughness $\bar{u}$ velocity contours (figure 10*a*) were uniform in the axial direction and decreased in the transverse direction in the expected (*a*) Square roughness ($\bar{u}/U_{ref}$). (*b*) Diamond roughness ($\bar{u}/U_{ref}$).

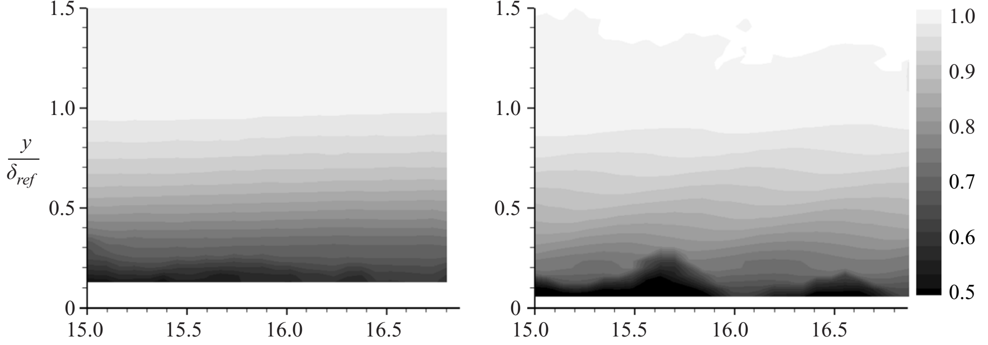

(*c*) Square roughness ($\bar{v}/U_{ref}$). (*d*) Diamond roughness ($\bar{v}/U_{ref}$).

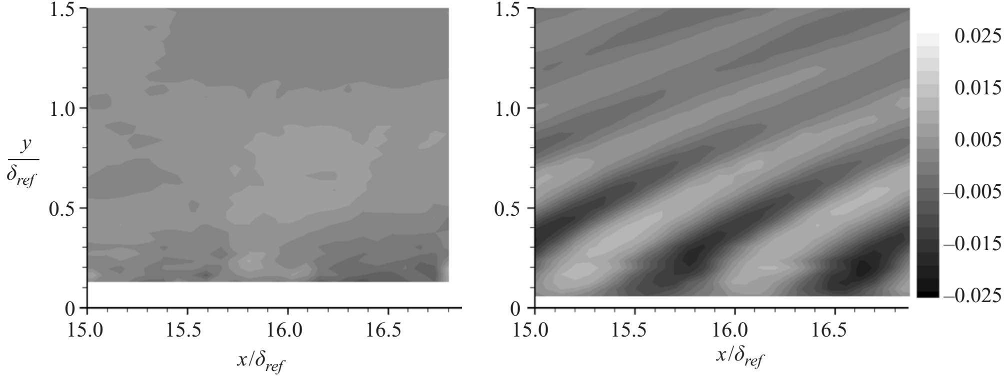

FIGURE 10. Zero pressure gradient rough-wall velocity (PIV) contours (location 1).

manner, while corresponding $\bar{v}$-components were very small. On the other hand, the $\bar{u}$-component contour plots for the diamond roughness exhibited a wavy pattern throughout the boundary layer and into the free stream. The pattern corresponded to shock and expansion waves generated by the roughness elements shown in figure 7(*b*). The low-velocity regions near the wall at $x/\delta_{ref} = 15.7$ and 16.6 were near the leading edge of a row of diamond elements. In addition, for the $\bar{v}$-component, a series of alternating negative and positive bands were observed, where the values varied between 0.02 and $-0.015U_{ref}$.

The strong favourable pressure gradient model transverse velocity results for the smooth, square and diamond roughness element plates are given in figure 11. The weak favourable pressure gradient results were very similar to the zero pressure gradient results, and thus the contours are not reproduced here. However, the trends are included in the subsequent discussion. The mean transverse velocity component ($\bar{v}$) at the second station for the weak favourable pressure gradient model was nominally $-0.02U_{ref}$ for both the smooth and square surface roughness models, with similar trends exhibited at the third station. The only difference of note between the second and third stations was the larger turning angle, where $\bar{v} = -0.05U_{ref}$ for the smooth and $-0.04U_{ref}$ for the square roughness cases, which are in line with the steeper wall angle (see figure 5). The strong favourable pressure gradient smooth wall transverse velocities varied between -0.05 and $-0.15U_{ref}$ over the PIV interrogation window at the second station. The corresponding square roughness model boundary layer was thicker and the transverse velocity range was slightly smaller at -0.05 to $-0.12U_{ref}$.

(*a*) Location 2: $\bar{v}/U_{ref}$

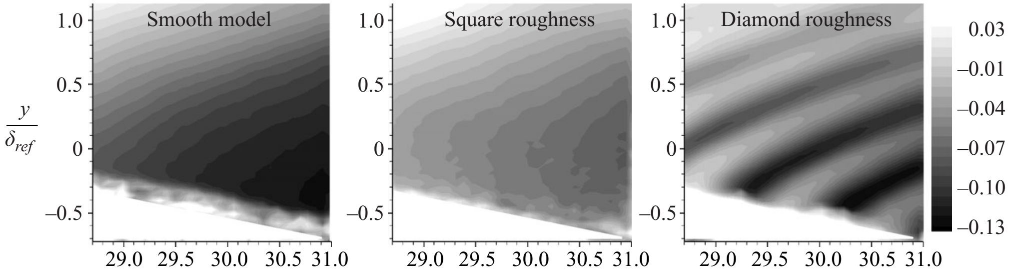

(*b*) Location 3: $\bar{v}/U_{ref}$

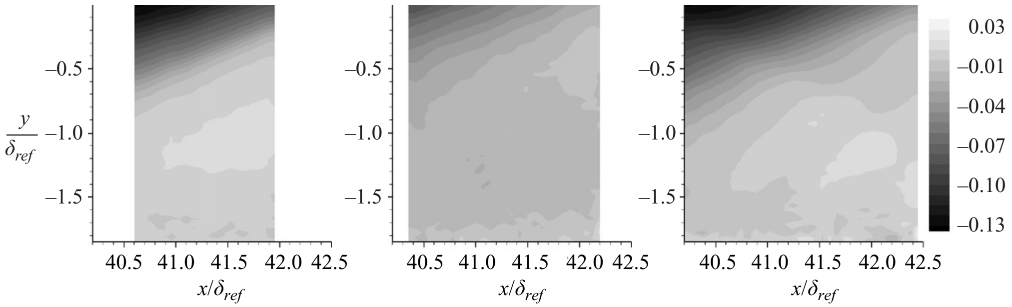

FIGURE 11. SFPG model transverse velocity (PIV) contours.

In contrast, by the combined pressure gradient region (figure 11*b*) the flow had resumed in the axial direction, as indicated by the nominally zero transverse velocity component. It should be noted, however, that in the upper left corner, which was located upstream of the recompression shock, the transverse velocity was still moving towards the floor. The axial velocity contours (not shown) were qualitatively similar for all three models and similar in structure to the upstream zero pressure gradient contours shown in figure 10(*a*) and (*b*). For the square model, a region of relatively low axial momentum was present in the lower 40 % of the boundary layer.

For the diamond roughness cases with favourable pressure gradients, the $\bar{u}$-component contour plots exhibited a wavy pattern similar to that observed in figure 10 for the zero pressure gradient models. Also, low-momentum regions were visible near the leading edges of two rows of elements at $x/\delta_{ref} = 29.2$ and 30.2 of the weak favourable pressure gradient and strong favourable pressure gradient models. The $\bar{v}$ contour for the second weak favourable pressure gradient region (not shown) displayed the same periodic pattern seen in figure 11; however, in the expansion region, the velocity range was from 0 to $-0.04U_{ref}$. If $\bar{v}$, due to streamline curvature estimated at $-0.02U_{ref}$, based on the smooth and square element roughness results, is subtracted from the weak favourable pressure gradient diamond roughness values element values of $\bar{v}$, a wave pattern resulted with a relative variation due to the roughness element that was similar to the zero pressure gradient case. Again, aside from the increase in flow-turning angle, the trends at the third region were qualitatively similar. For the strong favourable pressure gradient model at location 2, the variation observed between $\bar{v}$ ranged between −0.07 and $-0.15U_{ref}$. The greater peak-to-peak variation, relative to the zero pressure gradient case, indicated enhanced locally generated strain rates with the globally imposed pressure gradient. The enhanced strain rates will be discussed in more detail in the following section. For the combined pressure gradient region, the periodic nature of the transverse velocity component was noticeably absent for the diamond model.

3.6. *Section summary*

Diamond, *k*-type, roughness altered the flow in a manner that was significantly different than the square, *d*-type, roughness of comparable height and frontal blockage. Specifically, the diamond element shock and expansion waves had a measurable effect on the local surface pressure and mean flow field. The flow structure for the zero pressure gradient square roughness topology followed the sand grain behaviour described by Goddard (1959). When spatially averaged, the diamond element data also tended to collapse onto the law of the wall and defect law plots, with van Driest II (1951) compressibility scaling. The diamond element model collapse is not considered definitive as the averages were insufficient. Nonetheless, this tendency suggests that the average behaviour of the diamond element flow, even with the strong wave structure, is amenable to the engineering approximations described in § 1.2. The favourable pressure gradients strengthened the secondary flow structure for the diamond roughness elements. However, in the combined pressure gradient region, the sonic point evidently moved above the roughness height, and wave structure was absent. Thus, in this region, the *k*-type diamond elements were expected to behave more like their incompressible counterparts.

4. Response of the Reynolds stresses to the fluid element deformations

Turbulence stresses, in the measurement coordinate system, were computed from the PIV data for all of the cases studied. In this section, the response of the Reynolds shear stresses to the mean fluid element deformations is characterized. The normal stresses, in principal axes, are discussed in § 5. For the present discussion, the canonical flows were defined as the cases where the boundary-layer flow structure depends on the surface condition and/or pressure gradient in a global manner. Conversely, the non-canonical flows were defined as the cases where the local boundary flow structure was significantly altered by the wall topology. The canonical flows include all of the smooth wall cases, all of the square roughness cases and the diamond element case in the combined pressure gradient region. The non-canonical flows include the zero and favourable pressure gradient diamond element cases.

4.1. *Canonical flows*

The smooth wall and square roughness Reynolds shear stress profiles are compared in figure 12(*a*), where $\tau_{xy}/\bar{\rho}U_{ref}^2 = -\overline{u'v'}/U_{ref}^2$. The data were averaged in the axial direction over a distance of $\sim 1.6 \cdot \delta_{ref}$. The vertical lines represent the scatter in the shear stress data over the averaged region; as indicated, the scatter follows the uncertainty estimates in § 2.9. The smooth and square roughness Reynolds stresses followed the expected trends from the literature as shown in figure 1(*b*); recall that the wall shear stress was estimated from the turbulent shear stresses via the correlation in figure 1(*b*). The corresponding mean deformations across the boundary layers were computed from the PIV velocity data. The deformations were normalized by the root-mean-square (r.m.s.) of the strain rates (ζ). The Bradshaw (1974) distortion, individual velocity gradients, mean dilatation ($\bar{u}_{k,k}$), strain rate $S_{xy}[= 1/2(\partial\bar{u}/\partial\bar{y} + \partial\bar{v}/\partial\bar{x})]$ and spanwise vorticity were tabulated in the first nine columns of table 4 for $y/\delta = 0.15$, 0.4 and 0.6. Also, listed in column 10 are the Reynolds shear stresses at the same locations. The remaining columns in table 4 are discussed in § 5.

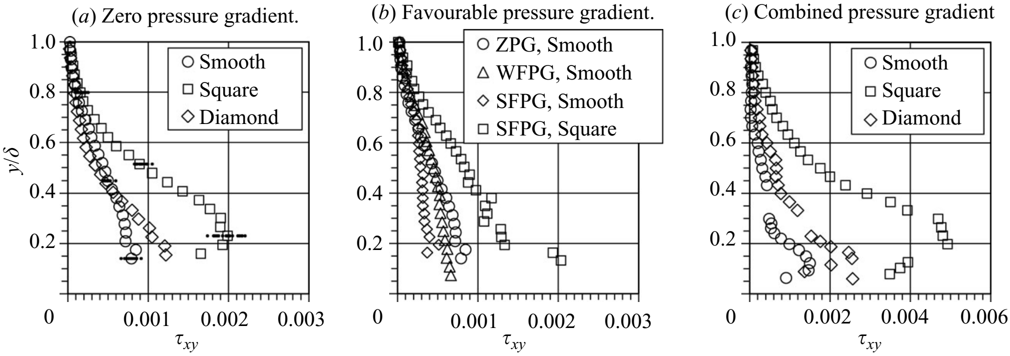

FIGURE 12. Reynolds shear stress profiles ($/\rho_{ref}U_{ref}^2$) in wind tunnel axes.

The overall structure of the deformation field for both the smooth and square roughness zero pressure gradient models is similar, where the principal strain rate dominated and the extra strain rates and dilatation were negligibly small; the values were within the experimental scatter. The only exception was a moderate near-wall distortion for the square roughness model due to the presence of an enhanced $\mathrm{d}\bar{v}/\mathrm{d}y$ gradient. This was most likely the result of the relatively weak waves visible in figure 7(*a*). Hence, the observed amplifications of the turbulence levels were attributed to the increased form drag on the roughness elements, as described by Goddard (1959). Collectively, the small dilatation, weak shocks (figure 7*b*) and Reynolds stress scaling in figure 1(*b*) suggest the validity of Morkovin's hypotheses for the square roughness model. Moreover, the shear stress and deformation results suggest that *d*-type roughness effects are amenable to numerical simulation through modification of the wall boundary condition with an effective sand-grain roughness height; e.g. the $k-\omega$ model as described by Wilcox (2000).

The smooth wall turbulent shear stress data, with the imposed curvature induced pressure gradients, followed previously established trends from the literature (§ 1.2), where the favourable pressure gradients had the expected stabilizing effect on turbulence stresses. As indicated in figure 12(*b*), the weak favourable pressure gradient effects were relatively modest, where, in the lower third of the boundary layer, the shear stresses were attenuated by 20 % with respect to the zero pressure gradient flow. Relative to the zero pressure gradient values, the strong favourable pressure gradient turbulent shear stress values were reduced by about 40 % in the lower half of the boundary layer. The corresponding strain rates are listed in table 4. In keeping with Bradshaw's (1974) definition for distortion, the values for *d* are presented in body normal coordinates, which required coordinate system rotations of -2.0°, -4.1° and -9.7° from the tunnel coordinate system for the weak favourable pressure gradient model at stations 2 and 3, and the strong favourable pressure gradient model at station 2, respectively. Imposing the weak favourable pressure gradient resulted in a 0.1 distortion strength across the boundary layer; this value was considered strong based on Bradshaw's (1974) criteria. The $\mathrm{d}\bar{v}/\mathrm{d}y$ velocity gradient was the major contributor to the flow distortion across the boundary layer. For the smooth wall strong favourable pressure gradient model, the total distortion values in the outer region were nominally 0.3–0.4. Flow stretching from the dilatation remained the primary contributor to *d* as $\mathrm{d}\bar{v}/\mathrm{d}y$ remained dominant. However, the $\mathrm{d}\bar{u}/\mathrm{d}x$ velocity gradient also made a significant contribution. The $\mathrm{d}\bar{v}/\mathrm{d}x$ deformation was also significant, but its negative value resulted in a 25 %–40 % reduction in the overall

$\frac{y}{\delta}$	d	$\frac{d\bar{u}}{dx}$	$\frac{d\bar{u}}{dy}$	$\frac{d\bar{v}}{dx}$	$\frac{d\bar{v}}{dy}$	$\bar{u}_{k,k}$	S_{xy}	Ω_z	$\frac{\tau_{xy}}{\bar{\rho}U_{ref}^2}$	$\frac{2k^T}{U_{ref}^2}$	$\left.\frac{\overline{u'u'}}{2k^T}\right\|_\lambda$	$\left.\frac{\overline{v'v'}}{2k^T}\right\|_\lambda$	α°	ϕ°	$\frac{2P\delta_{ref}}{\bar{\rho}U_{ref}^3}$	$\frac{(P_{xx})_\lambda}{2P}$	$\frac{(P_{yy})_\lambda}{2P}$	$\frac{(P_{xy})_\lambda}{2P}$
Zero pressure gradient – Smooth																		
0.15	−0.01	0.00	1.00	0.00	−0.01	−0.01	0.50	−0.50	0.0009	0.0066	0.87	0.13	−10.0	−0.4	0.00036	1.17	−0.17	−0.40
0.40	0.00	−0.01	1.00	0.00	0.00	−0.01	0.50	−0.50	0.0005	0.0028	0.88	0.12	−14.3	−0.2	0.00037	1.16	−0.16	−0.15
0.60	0.02	−0.01	1.00	0.00	0.03	0.02	0.50	−0.50	0.0003	0.0016	0.88	0.12	−12.7	−0.2	0.00015	1.17	−0.17	−0.20
Zero pressure gradient – Square																		
0.15	0.04	0.00	1.00	0.01	0.03	0.03	0.51	−0.50	0.0020	0.0382	0.82	0.18	−4.1	−0.4	0.00259	1.50	−0.50	−2.40
0.40	−0.02	−0.02	1.00	0.00	0.00	−0.02	0.50	−0.50	0.0016	0.0072	0.87	0.13	−12.7	0.3	0.00138	1.16	−0.16	−0.24
0.60	−0.01	−0.02	1.00	0.00	0.00	−0.02	0.50	−0.50	0.0007	0.0020	0.85	0.15	−11.9	0.3	0.00019	1.19	−0.19	−0.33
Weak favourable pressure gradient – Smooth																		
0.15	0.07	0.01	1.00	0.00	0.06	0.07	0.50	−0.50	0.0007	0.0050	0.87	0.13	−10.0	−1.6	0.00037	1.29	−0.29	−0.62
0.40	0.07	0.01	1.00	−0.01	0.06	0.07	0.50	−0.50	0.0005	0.0028	0.86	0.14	−15.2	−1.3	0.00020	1.29	−0.29	−0.27
0.60	0.10	0.01	0.99	−0.04	0.13	0.14	0.48	−0.52	0.0003	0.0019	0.85	0.15	−14.6	−1.0	0.00009	1.45	−0.45	−0.21
Weak favourable pressure gradient – Square																		
0.15	0.01	0.00	1.00	0.00	0.02	0.02	0.50	−0.50	0.0025	0.0405	0.92	0.08	−4.7	−2.0	0.00370	1.12	−0.12	−0.83
0.40	0.04	0.00	1.00	0.00	0.04	0.04	0.50	−0.50	0.0016	0.0088	0.84	0.16	−17.6	−1.6	0.00115	1.29	−0.29	−0.25
0.60	0.06	0.00	1.00	−0.01	0.08	0.08	0.50	−0.50	0.0007	0.0049	0.84	0.16	−16.0	−1.3	0.00044	1.35	−0.35	−0.26
Strong favourable pressure gradient – Smooth																		
0.15	0.08	0.06	0.99	−0.06	0.08	0.14	0.47	−0.53	0.0004	0.0057	0.74	0.26	−10.1	−8.9	-0.00018	0.65	0.35	1.70
0.40	0.32	0.05	0.92	−0.12	0.36	0.41	0.40	−0.52	0.0003	0.0023	0.76	0.24	−14.8	−7.6	-0.00007	−0.19	1.19	0.56
0.60	0.44	0.04	0.84	−0.18	0.51	0.55	0.33	−0.51	0.0003	0.0017	0.74	0.26	−12.4	−6.3	-0.00008	0.06	0.94	0.21
Strong favourable pressure gradient – Square																		
0.15	0.09	−0.01	0.99	−0.04	0.14	0.13	0.48	−0.52	0.0014	0.0162	0.74	0.26	−10.7	−7.3	-0.00025	−0.80	1.80	5.12
0.40	0.17	0.00	0.97	−0.06	0.24	0.24	0.46	−0.52	0.0010	0.0053	0.77	0.23	−18.2	−6.2	0.00005	5.84	−4.84	−3.43
0.60	0.26	−0.01	0.93	−0.11	0.36	0.37	0.41	−0.52	0.0006	0.0028	0.78	0.22	−13.8	−5.0	-0.00005	−1.17	2.17	1.05
Combined pressure gradient – Smooth																		
0.15	0.01	−0.01	1.00	0.00	0.02	0.01	0.50	−0.50	0.0015	0.0091	0.86	0.14	−12.7	−0.3	0.00172	1.21	−0.21	−0.30
0.40	−0.05	−0.04	1.00	0.02	−0.03	−0.07	0.51	−0.49	0.0005	0.0018	0.79	0.21	−27.9	0.2	0.00024	1.29	−0.29	0.00
0.60	−0.29	−0.06	0.94	0.10	−0.31	−0.37	0.52	−0.42	0.0003	0.0008	0.73	0.27	−24.9	−0.3	0.00010	1.10	−0.10	−0.35
Combined pressure gradient – Square																		
0.15	0.03	0.03	1.00	0.00	0.01	0.04	0.50	−0.50	0.0045	0.0341	0.82	0.18	−12.2	−2.2	0.00511	1.36	−0.36	−0.66
0.40	0.02	−0.01	1.00	0.01	0.02	0.01	0.51	−0.50	0.0021	0.0073	0.83	0.17	−21.7	−1.2	0.00130	1.26	−0.26	−0.07
0.60	−0.12	−0.02	0.99	0.06	−0.15	−0.17	0.53	−0.47	0.0010	0.0025	0.74	0.26	−33.5	−1.4	0.00041	1.30	−0.30	−0.06
Combined pressure gradient – Diamond																		
0.15	−0.03	−0.05	1.00	0.00	0.02	−0.03	0.50	−0.50	0.0025	0.0389	0.91	0.09	−4.4	−0.6	0.00852	1.08	−0.08	−0.37
0.40	−0.02	−0.04	1.00	0.03	−0.01	−0.05	0.52	−0.49	0.0007	0.0048	0.82	0.18	−21.5	−0.2	0.00095	1.23	−0.23	−0.10
0.60	−0.30	−0.06	0.94	0.09	−0.31	−0.37	0.52	−0.43	0.0003	0.0015	0.75	0.25	−29.9	−1.2	0.00030	1.13	−0.13	−0.20

Notes: (1) Columns $d\bar{u}/dx$ through Ω_z are normalized by ς; (2) the subscript λ indicates in-principal axes.

TABLE 4. Turbulence properties across the boundary layers.

flow distortion. Within the inner region, the distortion decreased by a factor of 5 relative to outer-region values, principally due to a significant decrease in $\mathrm{d}\bar{v}/\mathrm{d}y$. Luker *et al.* (2000) suggested that a strengthened $\mathrm{d}\bar{v}/\mathrm{d}x$ was the main contributor of extra production, but the current data suggest a complimentary effect, where all of extra deformations tended to be stabilizing.

The strong favourable pressure gradient velocity cases, listed in table 4, were the only ones that had a significant impact on the bulk dilatation and the S_{xy} strain rate. For all of the other cases, the dilation was negligible, and S_{xy} was nominally 0.5. For the smooth strong favourable pressure gradient, the trend for the bulk dilatation was that the magnitude became significantly larger with pressure gradient, and for the strong favourable pressure gradient, the mean dilatation was approximately 30 %–50 % of the principal strain rate. The S_{xy} strain rate decreased from 0.47 to 0.33, moving from the inner to outer regions of the boundary layer. From an eddy-viscosity modelling perspective, this would indicate a decrease in the Reynolds shear stress, with the most pronounced effect in the outer layer. When the present strong favourable pressure gradient data in figure 12(b) were expressed in body normal coordinates as described by Luker *et al.* (2000), the shear stress levels in the outer region were significantly reduced, which is consistent with the mixing length model. It is expected that the pressure work terms, which do not have incompressible counterparts, contributed to the turbulent shear stress transport dynamics. More specifically, the ratio of the pressure-work to production for the Reynolds shear stress was crudely estimated using the strong Reynolds analogy (Smits & Dussauge 1996). Accounting for axial pressure gradients and the primary $\mathrm{d}\bar{u}/\mathrm{d}y$ production component resulted in the following expression: $P_w/P \sim -[(\gamma-1)M^2](\tau_{xy}/\tau_{yy})(\rho_\infty U_\infty/\rho U)[(p-p_\infty)/\frac{1}{2}\rho_\infty U_\infty^2](\delta/L)$. For the present strong favourable pressure gradient model, the first term in this expression was ~ 4.0, the second two were both order 1.0, the pressure coefficient was 0.07 and the last term was ~ 0.5. Thus, the pressure-work to production ratio was roughly a modest 15 %.

Coupling the square roughness with the favourable pressure gradients introduced a competition between the destabilizing roughness and stabilizing pressure gradients. For example, the smooth wall and square surface roughness model distortions in the strong favourable pressure gradient region were similar in the inner boundary-layer region. However, the contributions from the individual gradients differed. Specifically, the rough-wall axial deformations, including the stabilizing $\mathrm{d}\bar{v}/\mathrm{d}x$, were significantly reduced, while $\mathrm{d}\bar{v}/\mathrm{d}y$ increased by 75 %. In the outer region, the square roughness distortion was 40 % lower than the corresponding smooth wall value. The net effect was reduced changes in the mean dilatation and S_{xy}. The results of these competing effects are apparent by comparing the square roughness Reynolds shear stress surveys in figures 12(a) and 12(b). Near the wall, the strong favourable pressure gradient Reynolds stress values were similar to the zero pressure gradient levels. However, farther in the boundary layer, a decline in turbulent shear stress relative to the zero pressure gradient model was observed, with reductions on the order of 50 %. These combined effects require a reasonable degree of inherent fidelity in a turbulence model to duplicate the intricate Reynolds stress–strain rate relationship for this case. Moreover, the pressure-work to production ratio is expect to have been enhanced by the roughness as Latin & Bowersox (2000) have shown that the correlation between the density and velocity fluctuations increased with increasing roughness height. Thus, the pressure-work was considered important in generating turbulence for this flow. However, the exact role was not considered any further as direct measurements were not achieved in this study. Overall, even with these shortcomings, it is believed that current two-equation turbulence models that treat this roughness topology via a modified boundary condition will capture the overall trends associated with the competing effects provided that appropriate compressibility corrections are included.

The shear stress profiles from the combined pressure gradient region are given in figure 12(*c*). The changes in the turbulent stress profile for the combined pressure gradient region indicated that the turbulent stress was dependent on the proximity to the dual sources of flow strain, the principal strain rate and the recompression. The corresponding velocity gradient data are listed in table 4. The sign of all extra strain rates was reversed as compared to the favourable pressure gradient location. This resulted in a negative overall distortion. The distortion values near the wall were much weaker than those in the outer region, where in the outer region, flow turning from the recompression shock was more pronounced. In the inner region, the bulk dilatation/compression was essentially zero small. However, in the outer region, the flow elements were significantly compressed and the vorticity was reduced.

The Reynolds shear stresses for the rough-wall combined pressure locations are also shown in figure 12(*c*). The square roughness and adverse pressure gradient coupled to produce turbulent shear stress levels that were 400 % above the smooth wall values. The profile shape for this case also had a peak that occurred near $y/\delta = 0.3$. For the combined pressure gradient diamond roughness model, the profile shape for the turbulent shear stress was similar to that of the smooth and square roughness case; however, the levels were nominally 40 % lower than the square roughness model. These lower turbulence levels were expected, as the skin friction at the wall was primarily a function of the roughness element drag (Liepmann & Goddard 1957) and the drag coefficient for the streamlined diamond topology was expected to be lower than that for the blunt square shapes. Also implicit in this argument are the assumptions that Townsend's scaling (1976) holds and the turbulence levels responded to the local surface condition. Adding roughness had minimal effects on the compression, S_{xy} and vorticity for the combined model as it did for the favourable pressure gradient models.

4.2. *Non-canonical flows*

The diamond element surface roughness models for the zero and favourable pressure gradient cases produced Reynolds shear fields that had a systematic dependence on the relative location to the surface topology. To demonstrate the nature of the flow, contours of the Reynolds shear stress and the $\mathrm{d}\bar{v}/\mathrm{d}y$ gradient for the zero and strong favourable pressure models are presented in figure 13. To better quantify the flow behaviour, axial plots of the deformation and distortions at $y/\delta = 0.15$, 0.4 and 0.6 are given in figure 14; the symbol legend is in the rightmost plot in figure 14(*a*). The left ordinate scale corresponds to the distortion, and the strain rates, normalized by the total strain rate, are on the right. The weak favourable pressure gradient cases were excluded from the present discussion, as their results can be inferred from the trends presented in table 4 and figure 14. For the zero pressure gradient model at $y/\delta = 0.15$, the deformations appear erratic. This was not surprising as the flow near the leading edges of the roughness elements showed signs of a localized disturbance (see figure 11). Additionally, laser wall reflections had a greater influence closer to the wall and possibly affected the results (see figure 6).

Traversing from left to right, for the zero pressure gradient flow in figure 13, the flow crossed the roughness element leading-edge shocks, which caused a band of negative $\mathrm{d}\bar{v}/\mathrm{d}y$ and increased turbulence shear stresses. The leading-edge shear stress increases were the result of shock–turbulence interactions and the subsequent

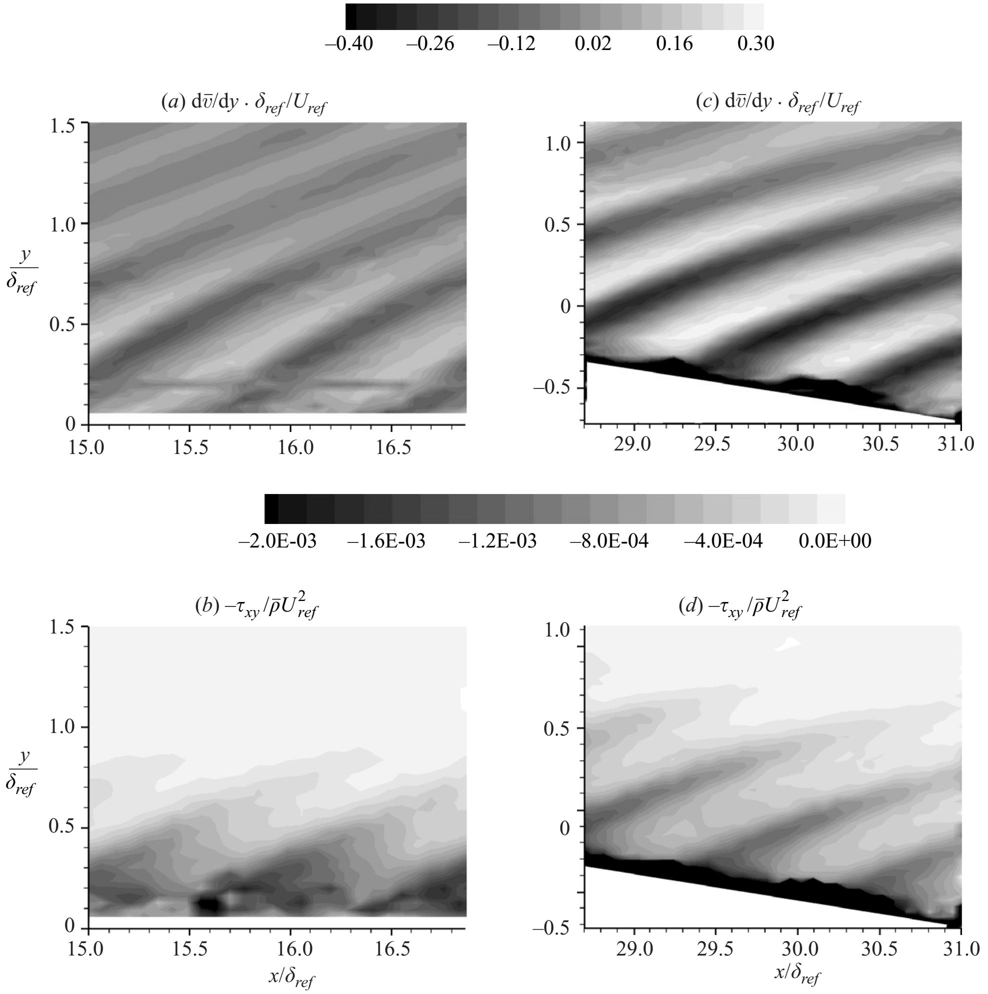

FIGURE 13. Strain-rate and Reynolds shear stress fields for the zero (left images) and strong favourable (right images) pressure gradient models with diamond roughness.

adverse pressure gradient on the front half of the roughness element (see figure 8). Farther downstream, the strain rate changed sign and the turbulence levels decreased. This decrease was the result of the local favourable pressure gradients on the back half of the roughness elements (see figure 8). Therefore, in the axial direction, the Reynolds shear stress had a periodic variation, where the minima values were on the order of the smooth wall models, while maxima values were doubled. The rapid response of the Reynolds shear stress to the strain-rate field indicated that linear effects were predominant in the transport dynamics. The corresponding distortions in figure 14 varied between ± 0.4, with the negative distortions corresponding to the adverse pressure gradient just after the roughness element leading edge, while the positive distortions resulted from the favourable pressure gradient generated by the roughness element trailing-edge expansions. The distortion behaviour was strongly coupled to $d\bar{v}/dy$, as $d\bar{u}/dx$ and $d\bar{v}/dx$ tended to cancel. The mean dilatation and S_{xy} tracked the distortion, and the vorticity was nominally constant at -0.5.

(*a*) Zero pressure gradient.

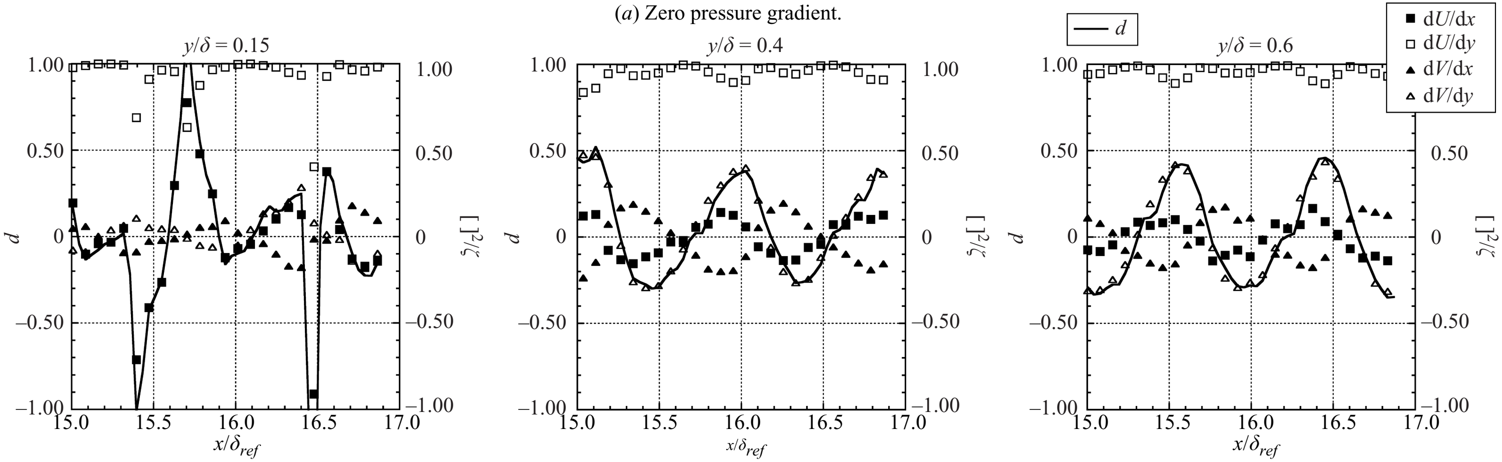

(*b*) Strong favourable pressure gradient.

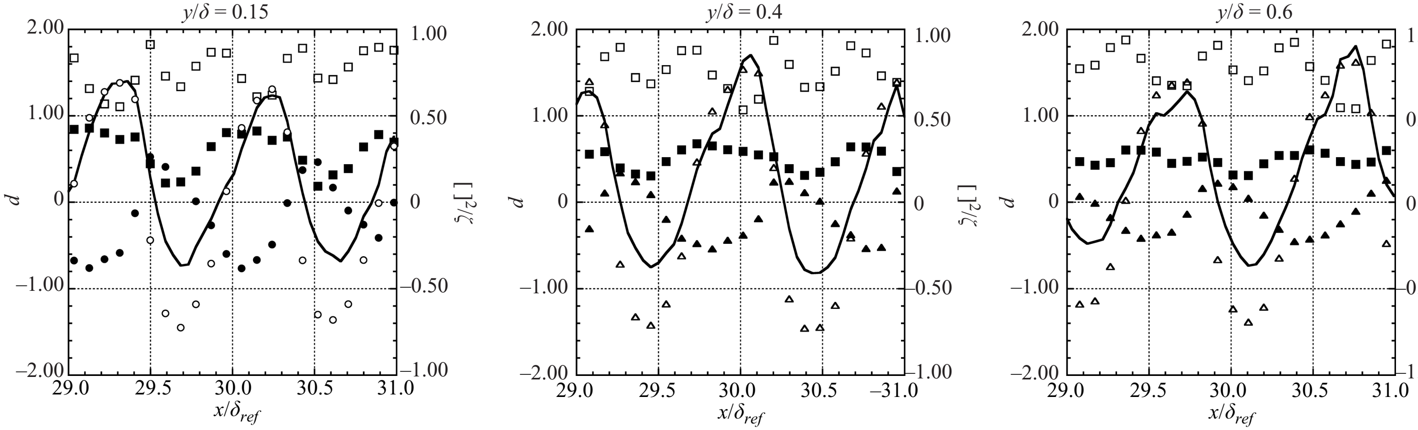

FIGURE 14. Axial profiles of diamond roughness model flow distortions.

For the strong favourable pressure gradient model, the global pressure gradient coupled with the local gradients generated by diamond roughness elements to produce a highly stratified (in the axial direction) shear stress field; see figure 13. As with the zero pressure gradient case, relatively large shear stress levels were observed near the leading-edge shock. In between the shock, the turbulence was highly damped by the presence of the global and local expansions, where the Reynolds stresses were reduced to values below those of the zero pressure gradient smooth wall boundary layer. The large shear stress levels at the leading edge demonstrated that shock–turbulence interaction was a dominant shear stress producing feature in this flow. The data in figure 14(*b*) demonstrated that the global favourable pressure gradient amplified all distortions, both positive and negative. For example, the distortions varied from −0.75 to 1.45. The mean dilatation peaks varied from −0.5 to 1.0. The S_{xy} strain rate varied from 0.25 to 0.45, where the minimum corresponded to the peak distortion, and the vorticity was nominally constant at −0.45. These changes likely were primarily due to a decrease in the overall strength of the principal strain rate ($\mathrm{d}\bar{u}/\mathrm{d}y$), and enhanced extra strain rates due to the orientation of the wall normal with the shock and expansion waves. Supporting evidence comes from the Schlieren image in figure 7(*b*), where the shock waves generated by the diamond element surface roughness became almost normal to the wall, and thus contributed little to the wall-normal principal strain rate while enhancing the extra velocity gradients.

The data in figure 13 indicated that the Reynolds shear stress responded strongly to the local distortions, which implied that the local effects appeared to prevail over history effects. The corresponding intricate Reynolds stress/strain-rate relationships imply that numerical simulations must resolve the flow structure within the roughness topology to accurately capture the flow structure. The pressure work terms were expected to be more important for this case, as compared to the global gradient cases, because similar pressure changes were observed over a smaller spatial extent, $\delta/L \sim 2$. As was the case in the previous section, the exact role was not considered any further as direct measurements were not achieved. However, it was observed that magnitude of the local Reynolds stress response to the local strain rates followed the pattern indicated by the canonical flows. This result suggests that current two-equation turbulence models with suitable compressibility corrections should capture the local trends.

4.3. *Section summary*

The Reynolds stress response to the canonical flow deformations behaved in an expected manner. For the zero pressure gradient square roughness case, compressibility effects were minimal and the flow structure across the boundary layer appeared to scale with the roughness surface condition as described by Townsend (1976). Hence, this case appears to be amenable to current prediction methods. The Reynolds stress response to the local strain rates followed the expected trend, where, as indicted by Bradshaw (1974), the distortions affected the flow by an order of magnitude more than would be anticipated by the associated extra production. This result suggests that current two-equation, or higher, turbulence models with suitable compressibility corrections may capture the correct trends. Collectively, the results in § 4.1 suggest that modern models may capture the competing roughness and pressure gradient effects for the canonical cases with square roughness.

The diamond element roughness produced local flow phenomena that altered the local state of the boundary layer, representing a marked departure from the canonical flows. The intricate Reynolds stress/strain-rate relationship implies that numerical

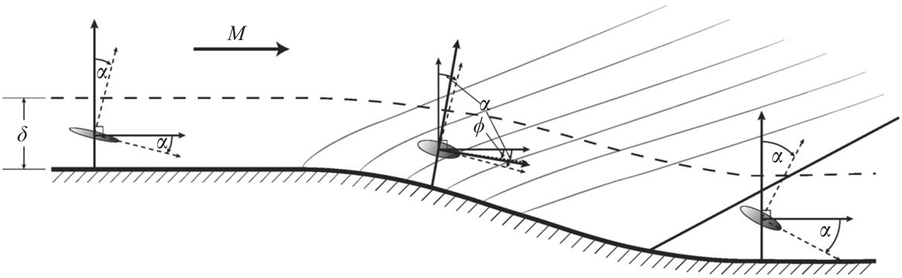

FIGURE 15. Turbulence stress orientation evolution.

simulations should resolve the flow within the roughness topology to accurately capture the overall structure. The magnitude of the local Reynolds stress response to the local strain rates followed the pattern indicated by the canonical flows. This result suggests that current turbulence models with suitable compressibility corrections may capture the local trends. These findings motivate the examination of the turbulence production and evolution mechanisms discussed in § 5.

5. Discussion of the turbulence evolution and production

The intricate Reynolds stress/strain-rate relationships described in the previous section for both the canonical and non-canonical flows motivated a closer examination of the turbulence production and evolution mechanisms. To help facilitate the discussion, an idealized representation of turbulence stress orientation evolution for the strong pressure gradient model is shown in figure 15. The ordinate for the wall coordinate system is represented by the arrow originating along the floor, which, for the first and third measurement locations, corresponds to the test section coordinate system. The dashed axes at each location represent the principal axes for the turbulent stress at $y/\delta = 0.4$. The turbulent stress-turning angle α is the rotation angle from the test section coordinate system to the turbulence stress principal axes. The ellipsoids illustrate the allocation and orientation of the principal stresses. The test section coordinate system is shown for reference at the second measurement location. Similarly, at the second test location, the flow-turning angle ϕ represents the rotation angle from the test section coordinate system to the axis along the mean velocity vector. This was omitted from the axes at locations 1 and 3 since, as will be seen later, the mean velocity vector was nearly aligned with the axial direction.

The turbulence stress principal axes were not known *a priori*. Thus, the data were collected in the test section coordinate system and transformed to their principal stresses via the coordinate transformation given in (5.1*a*)–(5.1*c*), with the condition that $\overline{u'_\lambda v'_\lambda}$ is equal to zero:

$$\overline{u'_\lambda u'_\lambda} = \overline{u'u'}\cos^2\alpha + 2\overline{u'v'}\cos\alpha\sin\alpha + \overline{v'v'}\sin^2\alpha, \tag{5.1a}$$

$$\overline{v'_\lambda v'_\lambda} = \overline{u'u'}\sin^2\alpha - 2\overline{u'v'}\cos\alpha\sin\alpha + \overline{v'v'}\cos^2\alpha, \tag{5.1b}$$

$$\overline{u'_\lambda v'_\lambda} = (\overline{u'u'} - \overline{v'v'})\cos\alpha\sin\alpha + \overline{u'v'}(\cos^2\alpha + \sin^2\alpha). \tag{5.1c}$$

For the present study, the measured k^T values were defined as $\frac{1}{2}(\overline{u'u'} + \overline{v'v'})$. Neglecting the lateral velocity gradients, the production terms were calculated in principal axes as follows:

$$(P_{xx})_\lambda \approx 2(\tau_{xx})_\lambda(\partial\bar{u}/\partial x)_\lambda, \tag{5.2a}$$

$$(P_{yy})_\lambda \approx 2(\tau_{yy})_\lambda(\partial\bar{v}/\partial y)_\lambda, \tag{5.2b}$$

$$(P_{xy})_\lambda \approx (\tau_{xx})_\lambda(\partial\bar{v}/\partial x)_\lambda + (\tau_{yy})_\lambda(\partial\bar{u}/\partial y)_\lambda. \tag{5.2c}$$

The production of turbulent kinetic energy was normalized by $2\delta/\bar{\rho}U_{ref}^3$, while the production components were normalized by $2P$.

Summarized in table 4 (columns 11–19) are the turbulence kinetic energy, normal stress components, turbulent stress-turning angle α, flow-turning angle φ, the turbulent kinetic energy production and the production components for the canonical cases at three transverse measurement locations ($y/\delta = 0.15$, 0.4 and 0.6). As the weak favourable pressure gradient data were only slightly altered as compared to the zero pressure gradient data, they are omitted from the subsequent discussion; these data are included in table 4 for completeness. The corresponding non-canonical flow results are presented as line plots parallel to the roughness elements at the same transverse locations as listed in table 4.

5.1. *Canonical flows*

As indicated by comparison of the first and second rows in table 4, adding the square roughness topology led to significant increases in the near-wall turbulent kinetic energy, where a 480 % increase was observed at $y/\delta = 0.15$. Increased momentum loss at the roughness elements due to form drag is believed to be the major driver for the dramatic increase in k^T. With increasing distance from the wall however, the relative increase in k^T was reduced. Wall roughness also significantly increased the relative amount of the transverse kinetic energy near the wall. Specifically, at $y/\delta = 0.15$, 18 % of k^T was due to $\overline{v'_\lambda v'_\lambda}$ for the rough wall, where the corresponding smooth wall value was 13 %, indicating an increase in secondary turbulent flow structures near the roughness elements. The turbulent stress-turning angle (α) for the zero pressure gradient smooth wall model was rotated about $-12°$ from the test section coordinate system, while the local flow angle ϕ remained parallel with the wall, which agrees well with the smooth wall zero pressure gradient LDV data from Luker *et al.* (2000) and Latin & Bowersox (2000). While the orientation in the outer portion of the boundary layer was similar for both wall surfaces, α rotated significantly from $-10°$ to $-4.1°$ for the rough wall case at $y/\delta = 0.15$. The redistribution of the turbulence stress tensor away from shear and towards compression helps to explain the unequal modification of the turbulence stress measurements in the wind tunnel axes system, where the turbulence shear stress doubled and the kinetic energy increased fivefold.

The overall increase in production (P) for the square roughness zero pressure gradient model was in line with observed increases in k^T at all locations. The composition of P from $(P_{xx})_\lambda$ and $(P_{yy})_\lambda$ remained constant throughout the boundary layer for the smooth wall zero pressure gradient model, with production due primarily to the $(P_{xx})_\lambda$ term, while the $(P_{yy})_\lambda$ term resulted in a slight reduction in overall P. The composition of P for the square roughness zero pressure gradient model at the outer two locations was similar. However, the near wall $(P_{xx})_\lambda$ was larger and the stabilizing effect from $(P_{yy})_\lambda$ was also more substantial. The square roughness inner region $(P_{xy})_\lambda$ term was ~ 500 % greater than the corresponding smooth wall value, which indicated the roughness elements resulted in a highly anisotropic production tensor. Within the inner region $(P_{xy})_\lambda$ had a magnitude that was 240 % greater than the cumulative contributions from the normal production components. Thus, in this region the production tensor principal axes were misaligned with respect to the turbulence stress principal axes. These results are consistent with the idea that the principal near-wall production mechanisms are altered from the conventional bursting process typically seen for smooth wall boundary layers towards localized production driven by roughness element-induced flow structures such as wake vortices (Grass 1971). The increase in $(P_{xy})_\lambda$ near the wall is also relevant to the pressure–strain redistribution, where for example, Launder, Reece & Rodi (1975) argued the essential features of the rapid part of the pressure–strain is linearly proportional to the production anisotropy for low-speed flows. The smallness of the dilatation for this case suggests applicability. The additional data listed in table 4 may provide additional insight into the rapid pressure–strain via more general models. However, such efforts were not attempted here, where, instead, the focus was on directly measured quantities. Nonetheless, the observed modification of the pressure–strain redistribution may be important to accurately predict the turbulence stress component via a seven equation Reynolds stress transport model; this implication applies to all of the remaining canonical flow cases described below.

The curvature induced strong favourable pressure gradient had the expected effect of reducing the overall k^T for the smooth wall cases, where the percent changes were $-14\,\%$, $-18\,\%$ and $6.2\,\%$ at $y/\delta = 0.15$, 0.4 and 0.6, respectively. The turbulence within the strong favourable pressure gradient boundary layer was significantly more isotropic than the smooth zero pressure gradient case, where $25\,\%$ of k^T was due to $\overline{v'_\lambda v'_\lambda}$ and $75\,\%$ from $\overline{u'_\lambda u'_\lambda}$. This result agrees with the intermittency conclusions from Luker *et al.* (2000), where it was also concluded the turbulence length scales were reduced, and thus the fluctuation were more readily dissipated. The axial normal stress component production was significantly reduced, with a negative value near $y/\delta = 0.4$, which indicated that turbulence energy was being transferred back to the mean flow (Arnette, Samimy & Elliott 1996). The positive sign on the transverse stress production explains the relative increase in transverse shear stress as compared to the zero pressure gradient flow. In the strong favourable pressure gradient flow, the positive transverse production meant that this component was being directly energized by the mean flow, where for the zero pressure gradient case, the negative transverse production results in an energy flow from the turbulence to the mean flow, and the transverse energy fluctuations are the result of the cross coupling between the axial and transverse components (e.g. pressure–strain redistribution). The sign change of the shear stress production explains the overall reduction in the shear stress plots in figure 12(*b*). More intuitively, this shear reduction can be explained by again referring to figure 15 and the values of α in table 4. For the strong favourable pressure gradient model the difference between the principal stresses and the main flow direction (i.e. $\alpha - \phi$) was $-1.2°$, $-7.2°$ and $-6.1°$ at $y/\delta = 0.15$, 0.4 and 0.6 respectively. This separation was much less significant than the values of $-9.6°$, $-14.1°$ and $-12.5°$, observed for the zero pressure gradient smooth model. Thus, the compressive stresses exerted on the flow were enhanced while the shear was minimized. This was the direct result of the extra strain rates altering the production, and hence structure of the turbulence.

As with the zero pressure gradient models, adding surface roughness to the strong favourable pressure gradient models significantly increased k^T relative to the corresponding smooth wall models. Specifically, comparing the strong favourable pressure gradient rough and strong favourable pressure gradient smooth wall results, increases in k^T of $185\,\%$, $130\,\%$ and $65\,\%$, for $y/\delta = 0.15$, 0.4 and 0.6 were observed, respectively. This result suggests a competition between the global pressure gradient and the flow structure established by the roughness topology. Specifically, the roughness elements produce increased shear stress through form drag, and the favourable pressure gradient was working to damp the turbulence through the mechanisms described earlier. Hence, even though the strong favourable pressure gradient square roughness turbulence levels increased relative to the smooth strong favourable pressure gradient model, the levels were significantly lower than zero pressure gradient square roughness cases. The overall production and production components demonstrate this competition. Adding the roughness tended to slightly decrease the stress principal axis direction, with the largest change of -3.4° Near $y/\delta = 0.4$. The anisotropy for the rough strong favourable pressure gradient case was similar to that of smooth strong favourable pressure gradient case.

In the combined pressure gradient region of the smooth wall model, k^T was 38 % larger than the corresponding zero pressure gradient values at $y/\delta = 0.15$. However, for the outer two locations, the turbulence levels had not yet been amplified back to either the zero pressure gradient or strong favourable pressure gradient levels. This is understandable as the production of k^T at $y/\delta = 0.15$ was about an order of magnitude larger than in the outer regions. Thus, the recovery of k^T was slower in the outer regions. The lower outer region levels, relative to the upstream strong favourable pressure gradient values, imply that k^T continued to decrease axially beyond the strong favourable pressure gradient measurement location. The structural content of the turbulence at $y/\delta = 0.15$ was similar to that for the zero pressure gradient model. However, in the outer regions, the turbulence appeared to be more isotropic and the stress tensor principal axes angles were significantly lower. These trends are shown schematically in figure 15, where it can be seen that the turbulence went from highly anisotropic turbulence towards a more isotropic with a favourable pressure gradient, and back towards anisotropy once passing through the adverse pressure gradient. The production component values were similar to those from the zero pressure gradient case, and hence drove the turbulence back towards zero pressure gradient values. The trends for the two rough-wall combined pressure gradient models were similar to the smooth wall results with the addition of the enhanced production due to the roughness. The higher production for the diamond element model at $y/\delta = 0.15$ was attributed to the thinner boundary layers and steeper velocity gradients in this region.

5.2. *Non-canonical flows*

As noted previously in § 4.1, the diamond element surface roughness created strain-rate fields that locally altered turbulent stress phenomena. Contours of the Reynolds shear stress production, in test section coordinates, for the zero pressure gradient and strong favourable pressure gradient models are displayed in figure 16. The values were normalized by the reference length scale divided by the mean density and the cube of the reference velocity ($\delta_{ref}/\bar{\rho}U_{ref}^3$). In both images, there are black structures near the lower surface. These structures were the result of selecting the greyscale range to highlight the changes in the outer region boundary layer ($y/\delta > 0.2$). The near-wall production P_{xy} was comparatively much larger due to the strong principal strain rate and elevated turbulence levels due to the roughness elements. Both the zero and strong favourable pressure gradient models showed similar structure in the P_{xy} contours. The systematic positive and negative production regions are strikingly periodic. The dark regions (contour levels ~ -0.002) corresponded to increased production of the Reynolds shear stress due to the leading-edge shocks and the subsequent compressive

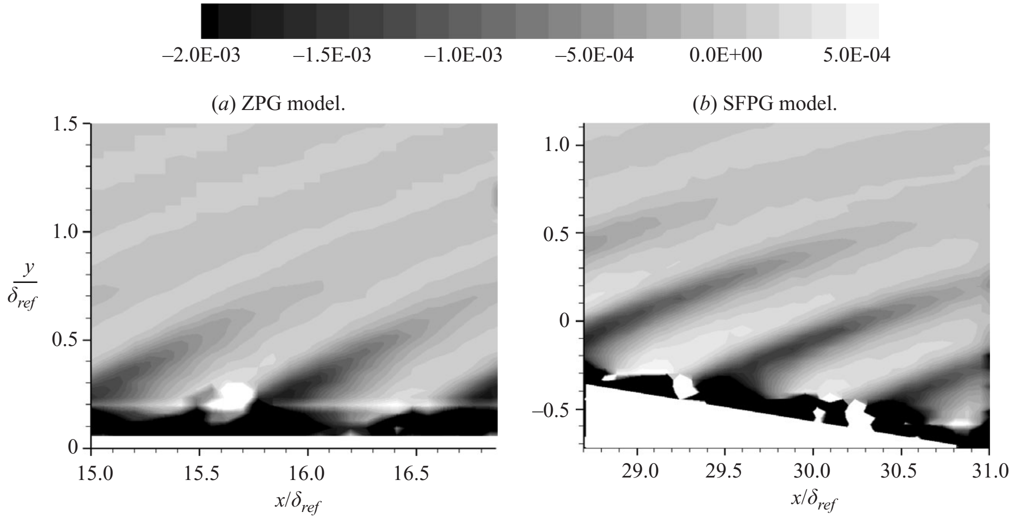

FIGURE 16. Diamond roughness element model turbulent shear stress production.

strain-rate field over the front half of the roughness element. In the light regions between the shocks, the production changed sign as the flow experienced stabilizing favourable pressure gradients along the aft half of the roughness element. The strong favourable pressure gradient model produced stronger shocks and larger regions of stabilization between the shocks. This result confirms that the shock–turbulence interactions were responsible for part of the turbulence level increases near the leading edge of the roughness element where, as described by Mahesh *et al.* (1997), the turbulence amplification across the shock depends on the angle between the shock and the shear layer. Hence, the amplifications varied across the boundary layer (see the curved shocks in figure 7*b*) and axially for the pressure gradient cases.

Line plots of the turbulence structure are given in figure 17 to better quantify the periodic nature of flow structure. The legend is in the rightmost plot in figure 17(*a*). The weak favourable pressure gradient cases were excluded, as the trends were similar to zero pressure gradient case. For the zero pressure gradient data in figure 17(*a*), k^T and α were observed to vary significantly at $y/\delta = 0.15$. These variations were due to the flow disturbances previously mentioned near the element leading edges. Although the $y/\delta = 0.15$ data are included for completeness, the subsequent discussion will be limited to the outer two locations. Focusing then on the data in figure 17(*a*) at $y/\delta = 0.4$ and 0.6, the overall average value of k^T was close to the smooth wall values, with a variation of $\pm 20\,\%$ and $\pm 10\,\%$ at $y/\delta = 0.4$ and 0.6, respectively. The sign of the variation depended on whether the datum point was in the local adverse or favourable pressure gradient region of the flow established by the surface element. However, the allocation of turbulent stress was nearly constant in the axial direction, with 85 % of k^T contained within $\overline{u'_\lambda u'_\lambda}$ for both locations. The principal stress axis angle exhibited strong variations between –10° to –20° in the favourable and adverse pressure gradient regions, respectively. On the present scale, the flow-turning angle appeared to be essentially constant. However, referring back $\bar{v}/U_{ref}$ contour (figure 10), the flow-turning angles were systematic as described in § 3.5.

Axial profiles of the production for the zero pressure gradient and strong favourable pressure gradient models are presented in figure 18 for $y/\delta = 0.15$, 0.4 and 0.6. The

(*a*) Zero pressure gradient.

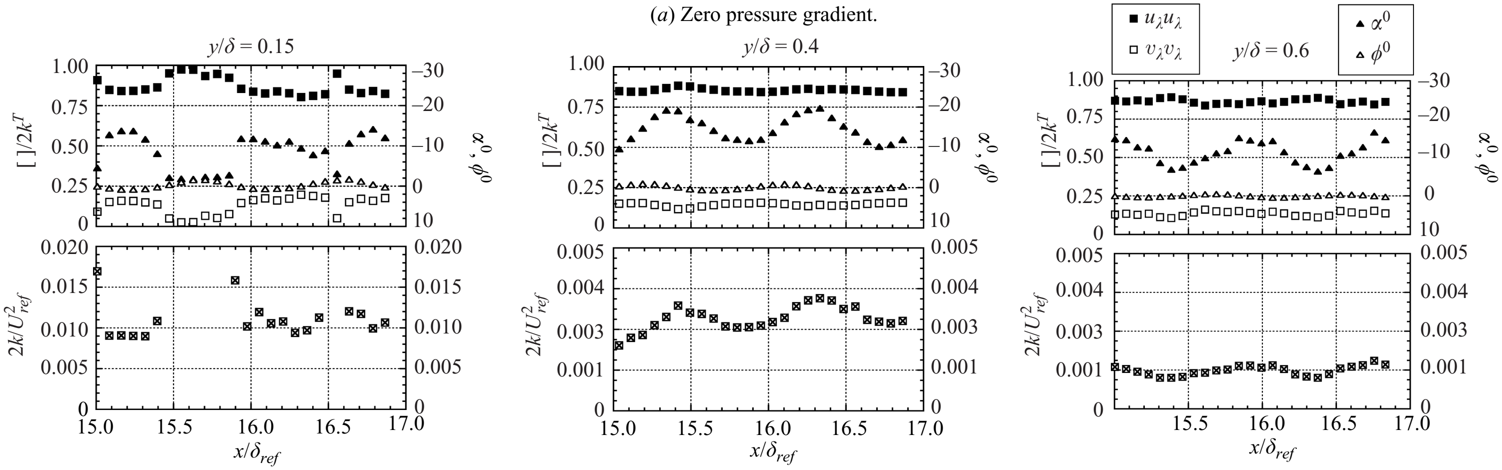

(*b*) Strong favourable pressure gradient.

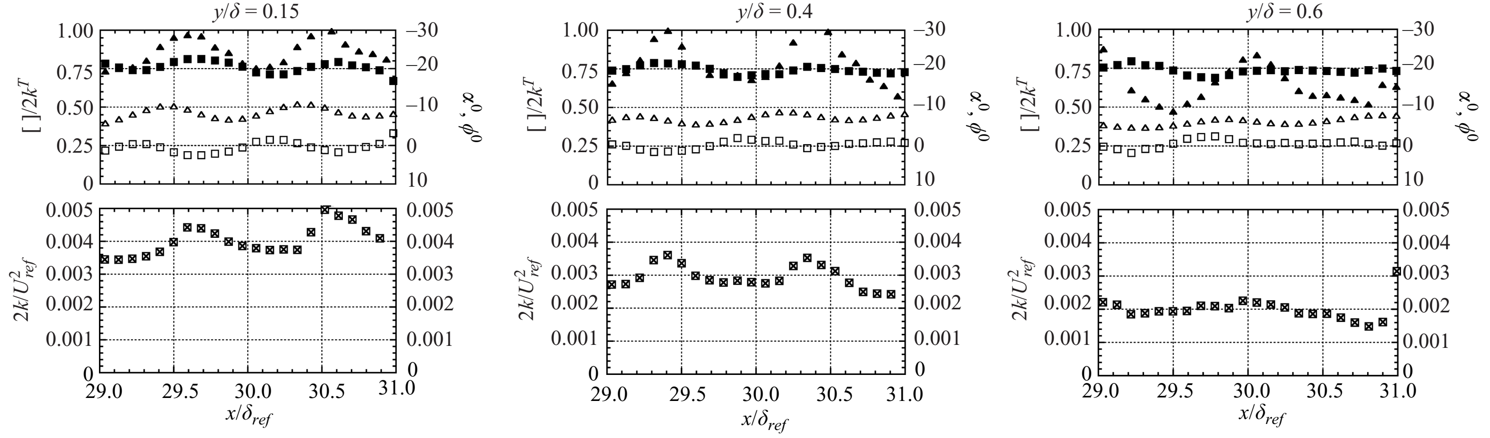

FIGURE 17. Axial profiles of diamond roughness turbulence stress.

(*a*) Zero pressure gradient.

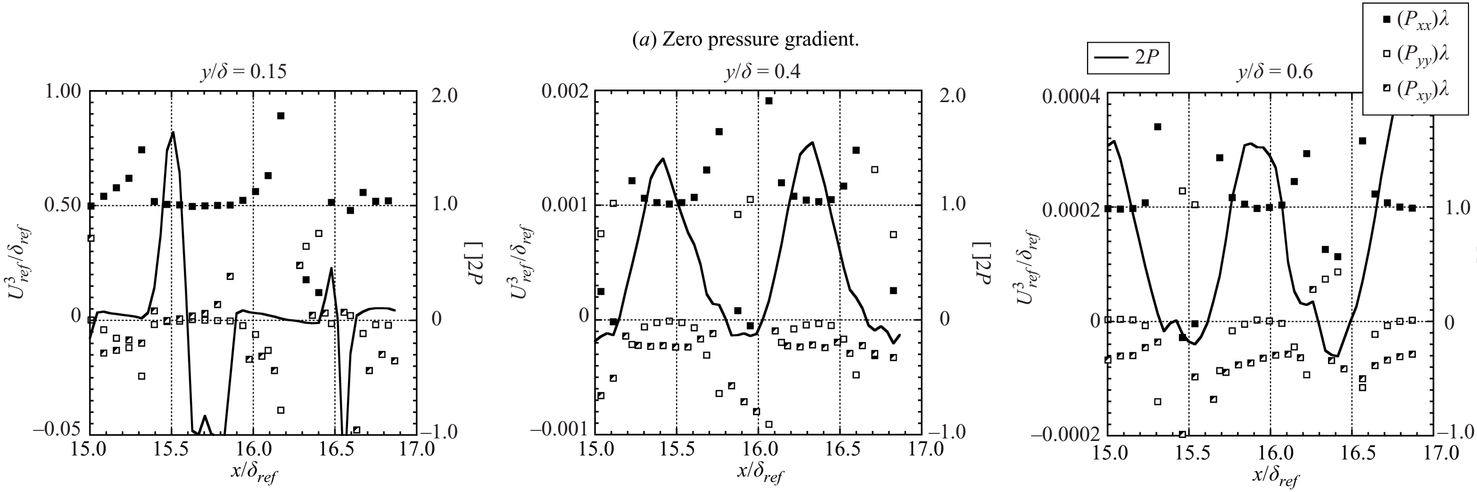

(*b*) Strong favourable pressure gradient.

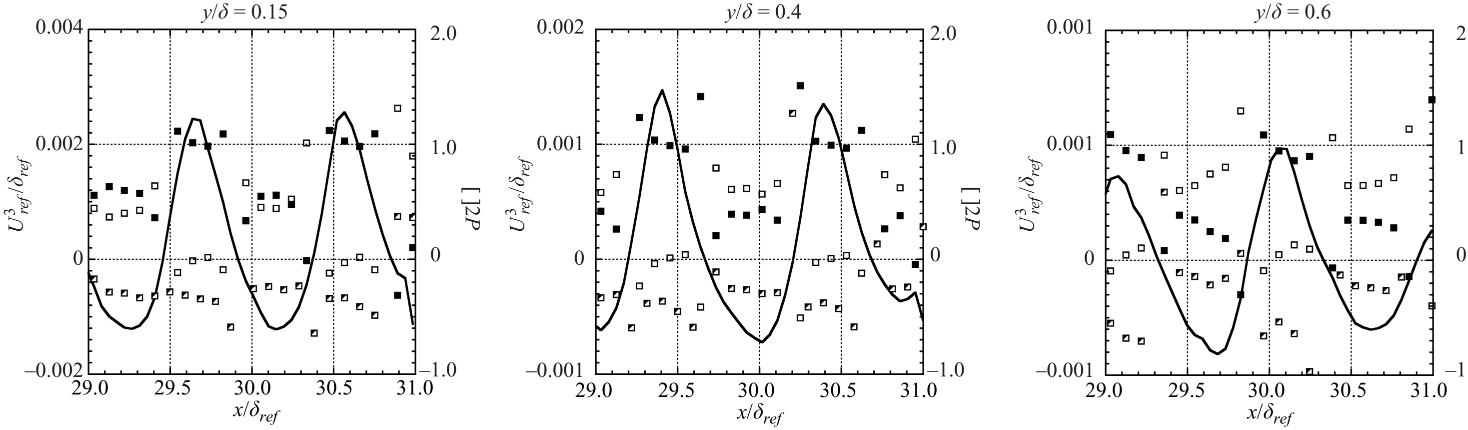

FIGURE 18. Axial profiles of diamond roughness model turbulent stress production.

nondimensionalization follows that in table 4. For each plot, the production of turbulent kinetic energy is on the left ordinate, while the production of the individual stresses is on the right. The legend is in the rightmost plot for the zero pressure gradient case. In the compression region for $y/\delta = 0.4$ and 0.6, the scalar production P had a maximum value that was similar in magnitude to that observed for the square surface roughness model at the same boundary-layer locations (in table 4). In the expansion regions, small pockets of negative production similarly existed. The $(P_{xx})_\lambda$ production term was dominant in the leading-edge compression regions. Conversely, the $(P_{yy})_\lambda$ term was dominant in the areas of negative production. Finally, the $(P_{xy})_\lambda$ term remained nearly constant at about 40 % of P at all boundary-layer locations. The observed production fields indicated an involved balance between production and redistribution, and this balance responded rapidly to the local flow distortions. It is likely that these intricate processes will have to be accounted for in order to accurately predict the turbulence stress component via a seven-equation Reynolds stress transport model. The rapid response to the local flow suggests that partially resolved methods, such as detached-eddy simulations, should prove useful, where only the shocks, expansions and flow structures shed from the elements are needed to be resolved.

The strong favourable pressure gradient model (figure 18*b*) also showed large periodic production across the roughness elements. The maximum values of P due to roughness element leading-edge compression were similar to those observed for the zero pressure gradient models. However, at the minima within the trailing-edge expansion regions, the production was about an order of magnitude more negative than for the zero pressure gradient case in figure 17(*a*). Profiles of the allocation of $(P_{xx})_\lambda$ and $(P_{yy})_\lambda$ had the appearance of complimentary positive and negative cosecant functions, where on average 75 % of P was due to the $(P_{xx})_\lambda$ term. Like the zero pressure gradient model, in the leading-edge compression regions, P was predominantly made up of the $(P_{xx})_\lambda$ term, while it was equally split between $(P_{xx})_\lambda$ and $(P_{yy})_\lambda$ in the expansion. The $(P_{xy})_\lambda$ production term also resembled a cosecant function that was in phase with $(P_{yy})_\lambda$. On average, $(P_{xy})_\lambda$ was about −70 % of the value of P, which was consistent with the values observed in the zero pressure gradient smooth wall inner region. The split between $(P_{xx})_\lambda$ and $(P_{yy})_\lambda$ retained the cosecant appearance exhibited in the inner region; however, the average split was around 65/35 for both of the outer points ($y/\delta = 0.4$ and 0.6). The distribution of $(P_{xy})_\lambda$ was similar to what was observed in the inner region.

5.3. *Section summary*

The near-wall flow structure and production mechanisms for the canonical zero pressure gradient square roughness model were significantly altered from the conventional bursting process towards localized production driven by roughness element-induced flow structures such as wake vortices (Grass 1971). The net effect was increased turbulence levels across the boundary layer. Near the wall, the principal stress axes orientation was significantly larger, which resulted in a redistribution of the turbulence stress tensor away from shear and towards compression. Also in this region, the production tensor was highly anisotropic, where the production tensor principal axes were misaligned with respect to the turbulence stress principal axes. These findings explain the unequal modification of the turbulence stresses measured in a wind axes system.

The strong favourable pressure gradient axial normal stress production was significantly reduced, with a negative value near $y/\delta = 0.4$, which indicated that turbulence energy from this component was being transferred back to the mean flow as suggested by Arnette *et al.* (1996). Conversely, the transverse normal stress production was positive for the strong pressure gradient flow, which meant that this component was directly energized by the mean flow. This behaviour is opposite to that of the zero pressure gradient flow. Thus, the overall transport dynamics were significantly altered including the cross-coupling between the axial and transverse components (e.g. pressure–strain redistribution). Coupling the roughness to the pressure gradients resulted in a competition between the global pressure gradient and the flow structure established by the roughness topology.

For the diamond models, the production was periodic, where production was positive and negative on the forward and aft half of the roughness elements, respectively. The coupled strong favourable pressure gradient model results confirmed that shock–turbulence interactions were responsible for part of the turbulence level increases near the leading edge of the roughness element. The overall flow structure and turbulence production varied significantly on a local scale. For example, the principal stress axis angle exhibited strong variations between −10° to −20° in the favourable and adverse pressure gradient regions, respectively. The scalar production had large maximum values near the leading edges (similar to the square roughness), where, in the expansion regions, negative production was seen. The component production varied across the element, where the axial production was dominant in the leading-edge regions; the transverse was dominant in the areas of negative production, and the shear stress production was nearly constant at about 40 % of scalar production across the element. Coupling the diamond and strong favourable pressure gradient had the net effect of increasing the spatial extent of the favourable pressure gradient region, which resulted in larger negative values of the scalar production, and a redistribution of the production components.

6. Concluding remarks

It was demonstrated in the present study that the local shock and expansion waves generated by small roughness elements ($k/\delta \sim 0.05$) can provide a mechanism to alter the mean flow field and turbulence structure across a boundary layer, which is fundamentally different from the subsonic flow. To better understand the response of the mean flow and turbulence to the roughness elements, a series of experiments were performed on a supersonic ($M = 2.87$) high-Reynolds-number boundary layer ($Re_\theta = 40\,000$). The two roughness topologies consisted of diamond- and square-shaped patterns. To provide a complete and relevant basis for analyses, experiments were performed under the same conditions and with the same instrumentation for the following cases: (1) zero pressure gradient boundary layer on a smooth wall, (2) zero pressure gradient boundary layer with square, canonical *d*-type, roughness topology, (3) zero pressure gradient boundary layer with diamond shaped *k*-type roughness topology, which produces a strong secondary flow structure through a pattern of attached oblique shocks and expansion waves, (4) favourable pressure gradient boundary layers on a smooth wall, (5) favourable pressure gradient boundary layers with square roughness, (6) favourable pressure gradient boundary layers with diamond roughness, (7) combined favourable then adverse pressure gradient boundary layer on a smooth wall, (8) combined pressure gradient boundary layer with square roughness, and (9) combined pressure gradient boundary layer with diamond roughness.

The purpose of the first two cases was to provide a canonical background for comparison purposes, where the *d*-type roughness was found to follow the subsonic trends. The purpose of case 3 was to characterize interactions between the local pressure waves and boundary-layer mean and turbulence flow structure. Cases 4, 5 and 7–9 were examined to characterize global distortion effects. The favourable pressure gradients in case 6 were selected to isolate and demonstrate the importance of shock–turbulence interactions near the leading edge of the roughness elements. The heights (0.8 mm) and the frontal blockage for both topologies were matched. To characterize the local interactions, the experimental data were acquired with sufficient resolution to characterize the mean and turbulence flow structure over individual roughness elements. Particle image velocimetry, pressure sensitive paint, Pitot pressure profiles and Schlieren photography were employed to achieve this experimental goal. An extensive database was achieved and analysed. A synopsis of the resulting basic flow processes is given below.

The diamond, *k*-type, roughness was shown to alter the mean flow in a manner that was significantly different than the square, *d*-type, roughness. Specifically, the diamond element shock and expansion waves had a measurable effect on the local surface pressure and mean flow field. The square roughness topology appeared to follow the sand grain behaviour described by Goddard (1959), where the velocity data followed the incompressible pattern with van Driest II (1951) scaling. When spatially averaged, the diamond element data also tended to collapse onto the law of the wall and defect law plots. These results indicated that the average behaviour of the diamond element flow, even with the strong wave structure, is amenable to the classical low-order engineering approximations. The zero pressure gradient square roughness Reynolds stresses, with Morkovin scaling (1961), for the smooth and square models collapsed onto the expected trend with Townsend scaling (1976), while the diamond element data did not. The magnitude of the square roughness Reynolds shear stresses near the wall was nominally 2.4 times that for the smooth wall, where, for the diamond model, the ratio was 1.3. This implies that skin friction was significantly lower for the diamond elements, which agrees with expectations based on Goddard's (1959) model.

The flow structure and production mechanisms for the canonical zero pressure gradient square roughness models were shown to be significantly different than the conventional bursting process typically seen for smooth wall boundary layers. Near the wall, the principal stress axes orientation was found to be significantly larger, which resulted in a redistribution of the turbulence stress tensor away from shear and towards compression. Also in this region, the production tensor was highly anisotropic, where the production tensor principal axes were misaligned with respect to the turbulence stress principal axes, explaining the unequal modification of the turbulence stresses measured in a wind axes system. Compressibility effects were found to be minimal and the flow structure across the boundary layer appeared to scale with the roughness surface condition as described by Townsend (1976). Hence, prediction of the overall trends for this case appears to be amenable to current two-equation prediction methods, where the roughness is treated by way of the boundary condition. However, the redistribution of the production tensor indicated a modification of the pressure–strain redistribution, which is believed to be important for accurate prediction of the turbulence stress components via a Reynolds stress transport model; this implication applies to all of the distorted canonical flow cases.

The smooth wall strong favourable pressure gradient production mechanism was significantly altered compared to the zero pressure gradient flow. Specifically, the strong favourable pressure gradient axial normal stress production was significantly reduced, with a negative value near $y/\delta = 0.4$, which indicated that turbulence energy from this component was being transferred back to the mean flow. Conversely, the transverse normal stress production was positive for the strong pressure gradient flow, which meant that this component was directly energized by the mean flow. This behaviour is opposite to that of the zero pressure gradient flow. Thus, the overall transport dynamics were significantly altered, including the cross-coupling between the axial and transverse components (e.g. pressure–strain redistribution). The Reynolds stress response to the local strain rates followed the expected trend, where, as indicted by Bradshaw (1974), the distortions affected the flow by an order of magnitude more than would be anticipated by the associated extra production. This result suggests that current two-equation, or higher, turbulence models, with suitable compressibility corrections, may have the necessary fidelity to capture the correct trends. Coupling the square roughness to the pressure gradient flows resulted in a competition between the global pressure gradient and the flow structure established by the roughness topology. The competition proceeded in an expected manner, suggesting that this flow may also be amenable to current prediction techniques. However, in addition to the production tensor redistribution mentioned in the previous paragraph, it was estimated that pressure-work terms were significant in the turbulence transport.

The diamond roughness element was found to produce local flow phenomena that altered the local state of the boundary layer. This was a marked departure from the canonical flows. The overall flow structure and turbulence production were found to vary significantly on a local scale. For example, the turbulent stress turning angle exhibited strong variations between −10° to −20° in the favourable and adverse pressure gradient regions, respectively. The scalar production had large maximum values near the leading edges (similar to the square roughness), where, in the expansion regions, negative production was seen. The component production varied across the element, where the axial production was dominant in the leading edge regions; the transverse production was dominant in the areas of negative production, and the shear stress production was nearly constant at about 40 % of scalar production across the element. Coupling the diamond and strong favourable pressure gradient had the net effect of increasing the spatial extent of the favourable pressure gradient region, which resulted in larger negative values of the scalar production, and a redistribution of the production components. The large leading-edge production results indicated that shock–turbulence interactions were responsible for part of the turbulence-level increases near the leading edge of the roughness element.

The observed intricate Reynolds stress/strain-rate relationship implied that the turbulence responded strongly to the local distortions, and thus numerical simulations must resolve the flow structure within the roughness topology to accurately capture the flow structure. The rapid response also indicated that linear effects were predominant in the transport dynamics. The magnitude of the local Reynolds stress response to the local strain rates followed the patterns indicated by the canonical flows, which suggests that current two-equation turbulence models with suitable compressibility corrections should capture the local trends provided the flow within the elements is resolved. The observed production fields indicated an involved balance between production and redistribution, and this balance responded in spatially rapid manner to the local flow distortions. Again, these intricate processes are most likely important for accurate prediction of the turbulence stress components via a seven-equation Reynolds stress transport model. Lastly, partially resolved methods such as detached-eddy simulation may be suitable for modelling these flows with strong local distortions, since these methods are capable of resolving shocks, expansions and flow structures shed from roughness elements.

This work was sponsored (in part) by the Air Force Office of Scientific Research, USAF, under grant/contract number F49620-02-1-0365. The views and conclusions contained herein are those of the authors and should not be interpreted as necessarily representing the official policies or endorsements, either expressed or implied, of the Air Force Office of Scientific Research or the U.S. government.

REFERENCES

Antonia, R. & Wood, D. 1975 Calculation of a turbulent boundary layer downstream of a small step change in surface roughness. *Aeronaut. Q.* 202–210.

Arnette, S. A., Samimy, M. & Elliott, G. S. 1996 The effects of expansion regions on the turbulence structure of compressible boundary layers. *AIAA Paper* 96-0656.

Benedict, L. H. & Gould, R. D. 1996 Towards better uncertainty estimates for turbulence statistics. *Exp. Fluids* **22**, 129–136.

Berg, D. 1979 Surface roughness effect on a Mach 6 turbulent boundary layer. *AIAA J.* **17** (9), 929–930.

Bons, J., Taylor, R., McClain, S. & Rivir, R. 2001 The many faces of turbine surface roughness. *J. Turbomach.* **123** (4), 739–748.

Bowersox, R. 1996 Combined laser Doppler velocimetry and cross-wire anemometry analysis for supersonic turbulent flow. *AIAA J.* **34**, 2269–2275.

Bradshaw, P. 1969 The analogy between streamline curvature and buoyancy in turbulent shear flow. *J. Fluid Mech.* **36**, 177–191.

Bradshaw, P. 1974 The effect of mean compression or dilatation on the turbulence structure of supersonic boundary layers. *J. Fluid Mech.* **63** (3), 449–464.

Dolling, D. S. 1990 Unsteadiness of supersonic and hypersonic shock induced turbulent boundary layer separation. AGARD R 704, Chapter 7.

Dussauge, J. P. & Gaviglio, J. 1987 The rapid expansion of a supersonic turbulent flow – role of bulk dilatation. *J. Fluid Mech.* **174**, 81–112.

Dussauge, J. P., Smith, R., Smits, A., Fernholtz, H., Finley, P. & Spina, E. 1996 Turbulent boundary layers in subsonic and supersonic flow. AGARDograph No. 335, NATO, Canada Communications Group, Hull (Quebec) Canada.

George, J. & Simpson, R. 2000 Some effects of sparsely distributed three-dimensional roughness elements on two-dimensional turbulent boundary layers. *AIAA Paper* 2000-0915, Reno, NV.

Goddard, F. 1959 Effects of uniformly distributed roughness on turbulent skin-friction drag at supersonic speeds. *J. Aero/Space Sci.* **26** (1), 1–24.

Grass, A. 1971 Structural features of turbulent flow over smooth and rough boundaries. *J. Fluid Mech.* **50**, 233–255.

Jacquin, L., Cambon, C. & Blin, E. 1993 Turbulence amplification by a shock-wave and rapid distortion theory. *Phys. Fluids* A **5**, 2539–2550.

Jimenez, J. 2004 Turbulent flows over rough walls. *Ann. Rev. Fluid Mech.* **36**, 173–196.

Keller, J. & Merzkirch, W. 1990 Interaction of a normal shock with a compressible turbulent flow. *Exp. Fluids* **8**, 241–248.

Klebanoff, P. May 1955 Characteristics of turbulence in a boundary layer with zero pressure gradient. Report 1247, National Committee for Aeronautics (and NASA TN 3178).

Latin, R. & Bowersox, R. 2000 Flow properties of a supersonic boundary layer with wall roughness. *AIAA J.* **38** (10), 1804–1821.

Latin, R. & Bowersox, R. 2002 Temporal turbulent flow structure for supersonic rough-wall boundary layers. *AIAA J.* **40** (5), 832–841.

Launder, B., Reece, G. & Rodi, W. 1974 Progress in the development of a Reynolds-stress turbulence closure. *J. Fluid Mech.* **68**, 537–566.

Liepmann, H. & Goddard, F. 1957 Note on Mach number effect upon the skin friction of rough surfaces. *J. Aero/Space Sci.* **24** (10), 784.

Ligrani, P. & Moffat, R. 1986 Structure of transitionally rough and fully rough turbulent boundary layers. *J. Fluid Mech.* **162**, 69–98.

Liu, T. & Sullivan, J. P. 2005 *Pressure and Temperature Sensitive Paints*. Springer.

Luker, J., Bowersox, R. & Buter, T. 2000 Influence of a curvature driven favorable pressure gradient on a supersonic turbulent boundary layer. *AIAA J.* **38** (8), 1351–1359.

Mahesh, K., Lele, S. & Moin, P. 1993 The response of anisotropic turbulence to rapid homogenous one-dimensional compression. *Phys. Fluids* **6** (2), 1052–1062.

Mahesh, K., Lele, S. & Moin, P. 1995 The interaction of an isotropic field of acoustic waves with a shock wave. *J. Fluid Mech.* **300** 383–407.

Mahesh, K., Lele, S. & Moin, P. 1997 The influence of entropy fluctuations on the interaction of turbulence with a shock wave. *J. Fluid Mech.* **334**, 353–379.

McClain, S., Hodge, K. & Bons, J. 2003 Predicting skin friction and heat transfer for turbulent flow over real gas-turbine surface roughness using the discrete element method. *GT2003–38813, Proceedings of the ASME Turbo Expo Power for Land, Sea and Air*. Atlanta GA.

Morkovin, M. 1961 Effects of compressibility on turbulent flows. In *The Mechanics of Turbulence* (ed. A. Favre), pp. 368–380. Gordon and Breach.

Navarra, K. R., Rabe, D. C., Fonov, S. D., Goss, L. P. & Hah, C. 2001 The application of pressure- and temperature-sensitive paints to an advanced compressor. *ASME Trans.* **123**, 823–829.

Nikuradse, J. 1933 Stromungsgesetze in rauhen rohren. *Forschg.-Arb. Ing.-Wesen.* No. 361.

Perry, A., Schofield, W. H. & Joubert, P. N. 1969 Rough wall turbulent boundary layers. *J. Fluid Mech.* **37**, 383–413.

Perry, A., Lim, K. & Henbest, S. 1987 An experimental study of the turbulent structure in smooth- and rough-wall boundary layers. *J. Fluid Mech.* **177**, 437–466.

Reda, D., Ketter, F. & Fan, C. 1975 Compressible turbulent skin friction on rough and rough/wavy walls in adiabatic flow. *AIAA J.* **13**, 553–555.

Raupach, M., Antonia, R. & Rajagopalan, S. 1991 Rough wall turbulent boundary layers. *Appl. Mech. Rev.* **44**, 1–25.

Schlichting, H. 1955 *Boundary Layer Theory*. McGraw-Hill.

Schultz, M. & Flack, K. 2007 The rough-wall turbulent boundary layer from the hydraulically smooth to the fully rough regime. *J. Fluid Mech.* **580**, 381–405.

Shockling, M., Allen, J. & Smits, A. 2006 Roughness effects in turbulent pipe flow. *J. Fluid Mech.* **564**, 267–285.

Simpson, R. 1973 A generalized correlation of roughness density effects on the turbulent boundary layer. *AIAA J.* **11** (2), 242–244.

Sinha, K., Mahesh, K. & Candler, G. V. 2003 Modelling shock unsteadiness in shock/turbulence interaction. *Phys. Fluids* **15** (8), 2290–2297.

Sinha, K., Mahesh, K. & Candler, G. V. 2005 Modelling the effect of shock unsteadiness in shock/turbulent boundary-layer interactions. *AIAA J.* **43** (3), 586–594.

Smith, D. & Smits, A. 1991 The rapid expansion of a turbulent boundary layer in a supersonic flow. *Theor. Comput. Fluid Dynam.* **2**, 319–328.

Smits, A. & Dussauge, J-P. 1996 *Turbulent Shear Layers in Supersonic Flow*. American Institute of Physics.

Smits, A., Spina, E., Alving, A., Smith, R., Fernando, E. & Donovan, J. 1989 A comparison of the turbulence structure of subsonic and supersonic boundary layers. *Phys. Fluids* A **1** (11), 1865–1875.

Spina, E., Smits, A. & Robinson, S. 1994 The physics of supersonic turbulent boundary layers. *Ann. Rev. Fluid Mech.* **26**, 287–319.

Thivet, F., Knight, D. D., Zheltovodov, A. A. & Maksimov, A. I. 2001 Insights in turbulence modeling for crossing-shock-wave/boundary-layer interactions. *AIAA J.* **39** (6), 985–995.

Townsend, A. 1976 *The Structure of Turbulent Shear Flow*, 2nd ed. Cambridge University Press.

Van Driest, E. 1951 Turbulent boundary layers in compressible fluids. *J. Aeronaut. Sci.* **26** (3), 287–319.

Wallin, S. & Johansson, A. V. 2000 An explicit algebraic Reynolds stress model for incompressible and compressible turbulent flows. *J. Fluid Mech.* **403**, 89–132.

Wilcox, D. 2000 Turbulence Modeling for CFD, 2nd Ed., DCW Industries, Inc.